VIETNAM NATIONAL UNIVERSITY, HANOI
UNIVERSITY OF SCIENCE
FACULTY OF PHYSICS

****

NGUYEN THI THAO

THE DETECTION OF EXTENSIVE AIR SHOWERS IN HANOI

MASTER THESIS

Hanoi - 2007

VIETNAM NATIONAL UNIVERSITY, HANOI
UNIVERSITY OF SCIENCE
FACULTY OF PHYSICS
****

NGUYEN THI THAO

THE DETECTION OF EXTENSIVE AIR SHOWERS IN HANOI

(GHI NHẬN MƯA RÀO KHÍ QUYỂN DIỆN RỘNG TẠI HANOI)

MASTER THESIS
NUCLEAR PHYSICS
CODE: 1.02.03

SUPERVISOR: Prof. PIERRE DARRIULAT

Hanoi - 2007

ACKNOWLEDGEMENTS

My deep gratitude goes first to Prof. Pierre Darriulat, supervisor of this thesis, for countless discussions, enormous help during my master studies. Without him this work would have not been possible.

My sincere thanks would especially go to Dr. Dao Tien Khoa, Dr. Vo Van Thuan and Dr. Dang Quang Thieu for their help and advice. I also thank my colleagues, Pham Ngoc Diep, Pham Thi Tuyet Nhung and Pham Ngoc Dong, who have been working cooperatively with me. Their discussions and suggestions have been very valuable and have helped me in improving my work.

I also wish to thank the professors of the Department of Nuclear Physics and of the Faculty of Physics for giving lectures and encouragements when I studied at Hanoi National University.

This thesis would have never happened without the impressive work accomplished by the Auger Collaboration. I would like to express my deep gratitude to Prof. Jim Cronin, Murat Boratav, Pierre Billoir, Tiina Suomijärvi, Antonio Insolia and Paul Sommers for their support, discussions and their interest in the progress of our group.

I would like to thank the French CNRS, CERN, RIKEN, the Rencontres du Vietnam, the Odon Vallet fellowships, the World Laboratory and the Ministry of Science and Technology for invaluable support.

I am indebted to my family and many of my dear friends who have been very patient for all the trouble that I may have caused over the time I was busy with this work.

TABLE OF CONTENTS

INTRODUCTION

The present work deals with questions related to the detection of extensive air showers at VATLY, a cosmic ray laboratory in Ha Noi.

The first chapter is devoted to a description of the method used to detect cosmic rays in the Pierre Auger Observatory with which VATLY is associated. It relies on the properties of the extensive air showers produced by cosmic rays when entering the air atmosphere. More specifically its surface detector consists of an array of Cherenkov counters that make it possible to measure the direction from which the cosmic ray is coming and, from the lateral extension of the shower on ground, to measure its energy.

A replica of an Auger Cherenkov counter has been constructed and assembled on the roof of VATLY. In order to get some familiarity with the technique of cosmic ray detection used in the Auger surface detector, we have surrounded this counter [1] with three smaller counters that are the object of the present study. The associated hardware is described in detail in Reference [2]. A general description of the apparatus is given in Chapter 2.

Chapter 3 describes a simulation of the Ha Noi detector. It includes simple models of both the low energy atmospheric showers accessible by the detector and of the detector itself. Its predictions depend on only a few adjustable parameters that will be tuned by comparing them with actual data.

Chapter 4 presents the data that have been collected and compares them with the predictions of the simulation. In particular it provides an estimate of the transverse size of the detected showers and predicts what should be the response of the main VATLY Cherenkov counter to the trigger provided by a triple coincidence of the three smaller counters that are the object of the present study.

A summary of the main results is given at the end together with some perspectives for future studies.

1. COSMIC RAYS AND THE PIERRE AUGER OBSERVATORY (PAO)

1.1 Cosmic rays: general properties

1.1.1 Energy spectrum and composition

Primary cosmic rays are charged particles (here, we do not include photons and neutrinos under this name) that travel in space with energies reaching of the order of 10^{11} GeV. The vast majority (~98 %) of these particles are fully ionized atoms, mostly protons, with the remaining fraction being primarily electrons [3]. Of the nuclei, 90% are measured to be protons, 9% are alpha particles and the remaining 1% heavier nuclei [4]. However, these abundance ratios are strongly energy dependent. The dependence of the differential flux of primary cosmic ray particles on energy is illustrated in Figure 1. It covers 32 orders of magnitude and is seen to obey an approximate power law [5] with an index that varies between 2.5 and 3.3. Modulations have been found in the form of changes of slope. While they are not understood in detail, they are related to thresholds associated with new sources becoming accessible. Indeed the magnetic fields existing at various scales, Earth, Solar system, Milky Way, shield the Earth from cosmic rays, introducing effective low energy cut offs in their spectrum. In Ha Noi, the so called "rigidity" cut-off caused by the Earth magnetic field amounts to 17 GeV. The change of slope referred to as the "knee", just above 10^6 GeV, is associated with the shielding effect of the galactic magnetic field [6]. Above this energy, cosmic rays are mostly of extragalactic origin and are isotropic (galactic cosmic rays being enhanced on the equator of the Milky Way). The so-called "ankle", just above 10^9 GeV, is not well understood. Above 10^{11} GeV, the spectrum is cut off by the so called GZK effect [7,8] associated with the photoproduction of pions (either free or in the form of nucleon resonances) on the photons of the cosmic microwave background.

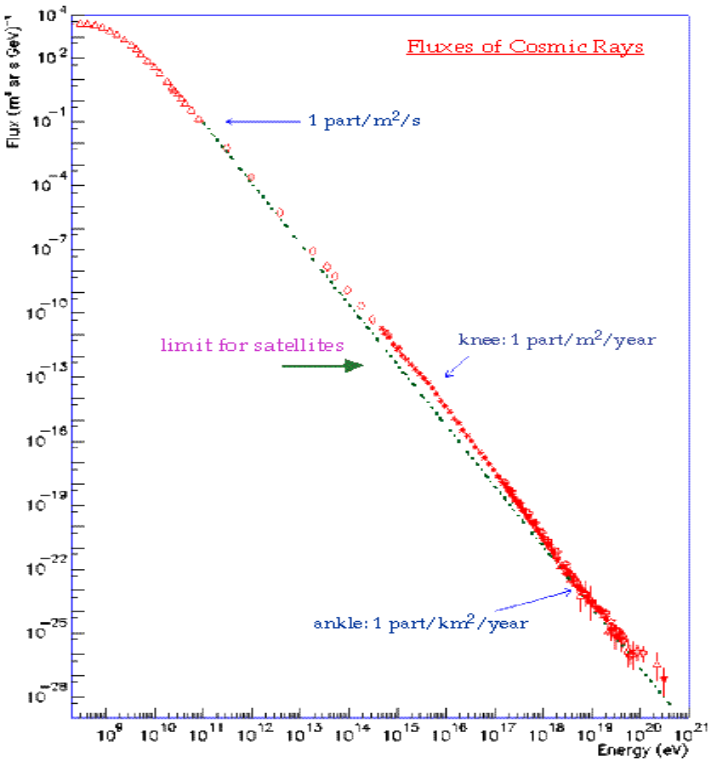

Figure 1. Differential primary energy distribution of cosmic rays.

1.1.2 Origin and acceleration mechanism

While the existence of cosmic rays resulting from the decay of very massive primordial particles cannot be fully excluded, it is generally considered that cosmic rays are the result of an acceleration mechanism acting on charged particles in space. One may distinguish between three different scales, solar, galactic and extragalactic.

At least part of the very low energy cosmic rays originate in the outer layers of the Sun, from what is called the solar wind. Some active regions of the Sun continuously emit particles with energies in the MeV range into interplanetary space and solar flares can sporadically accelerate particles up to several GeV/nucleon [9]. Above 0.1 GeV/nucleon, their contribution rapidly decreases. All stars are expected to emit stellar winds, in some cases significantly more energetic and with higher fluxes than the Sun. Their contribution to the cosmic ray spectrum extends to the TeV range or so.

In the 10^3 TeV range, cosmic rays are known to originate mostly from supernova remnants (SNR), as evidenced by the study of very high energy cosmic gamma rays in detectors such as HESS [10]. Such high energy photons are understood as being decay products of neutral pions produced by the interaction of very high energy cosmic rays with the interstellar matter present in the surroundings of their sources. The acceleration mechanism invoked to explain these very high energy cosmic rays is called “diffusive shock acceleration”. It is induced by multitraversals of the front of the shock wave produced at the time of the supernova explosion, by charged particles moving in a random walk in the magnetic fields present in the SNR environment. At yet higher energies, up to the GZK cut-off, it is usually believed that a similar mechanism is at play. The very high energies that may be reached place, however, very stringent constraints on possible sources that must be both very extended (compared to the magnetic bending radius) and the seat of strong magnetic fields (but in this context, “strong” may mean a few μG!). More concretely, it is the product of these two quantities that matters and the plot shown in Figure 2, the so-called Hillas plot, illustrates this fact in the case of 10^{11} GeV protons. First indications by Auger in favour of nearby AGN’s being the sources of ultra high energy cosmic rays have been recently presented [11, 12].

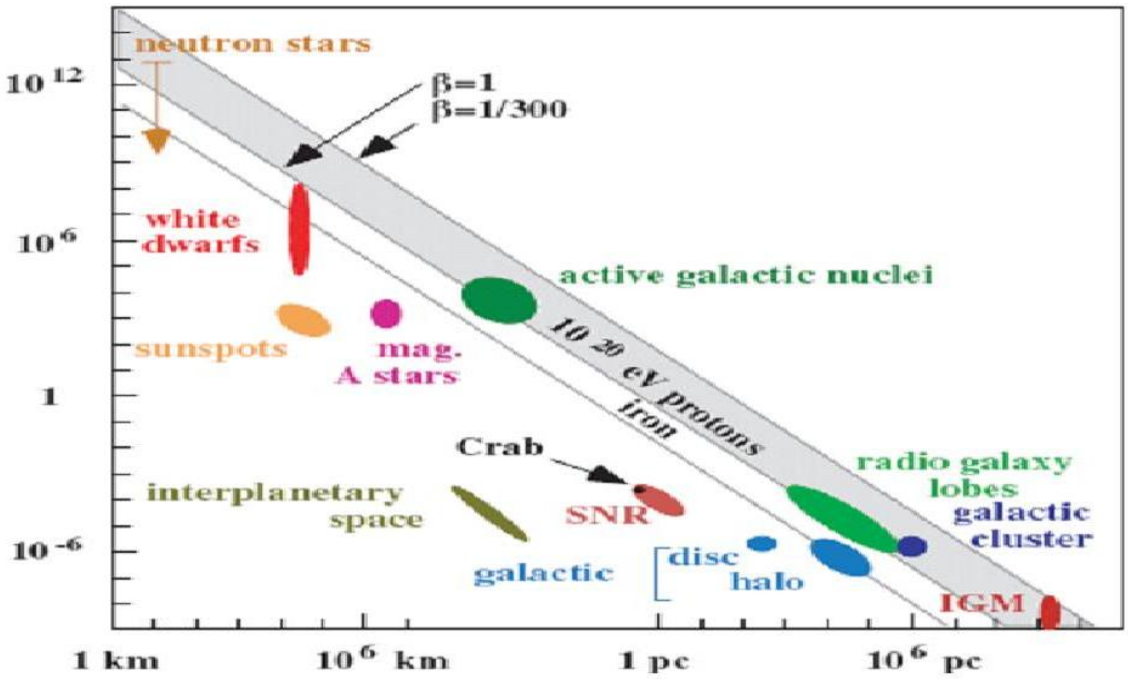

Figure 2. Hillas Plot showing the minimal value of the product BL (magnetic field × size) for accelerating a proton to 10^{20} eV. The limit is shown as a line in the logB(Gauss) − logL plot. A few candidate sites are indicated.

1.1.3 Air showers

When a cosmic ray enters the Earth atmosphere, it generates a hadronic shower (Figure 3). It develops at a scale defined by the nuclear interaction length of protons in air (90 g/cm^2). The atmospheric density decreases with altitude, approximately as an exponential having a decay length of 7.8 km. At very high energies, the multiplicity at each interaction is high as are the energies of the secondaries: the cascade develops very deep in the atmosphere. At the PAO, a 10^{11} GeV vertical shower is barely reaching its maximum when hitting ground, with several billions particles covering a few square kilometres. The difference between a proton induced shower and a shower induced by a heavier nucleus is mostly a faster early development in the second case as the nucleons in the nucleus can be thought of as interacting independently with air nuclei. At each interaction mesons are produced, mostly pions, kaons and their resonances, while the incident nucleon continues its way as a “leading” nucleon retaining a significant fraction of its energy (one talks of the inelasticity of the interaction as a measure of the difference between this fraction and unity). The mesons and meson resonances produced decay promptly with pions, either neutral or charged, as the main final hadronic product. While the neutral pions immediately decay into

two photons, and are therefore lost for continuing the hadronic shower development (they contribute instead to the development of an electromagnetic shower containing electrons, positrons and photons), the charged pions are not: they will often live long enough to interact with the air nuclei. The relevant factor measuring the competition between the two processes, interaction and decay, is the ratio between interaction and decay lengths (the latter multiplied by the very high gamma factor of the Lorentz boost). Charged pions decay into muons and neutrinos with a proper lifetime of 0.026 μs according to

$$\pi^{\pm} \rightarrow \mu^{\pm} + \nu_{\mu} \text{ (anti}\nu_{\mu}\text{)}.$$

Muons decay in turn into electrons and neutrinos, however with a much larger lifetime (2.2 μs).

When reaching ground, a very high energy shower is therefore dominated by its photon and electron component, the photons of the neutral pion decays having generated electromagnetic showers with a scale defined by the radiation length in air, 37 g/cm^2. The muon fraction is, however, strong enough to be detected and is observed to be a good discriminator between proton induced showers and showers induced by heavier nuclei.

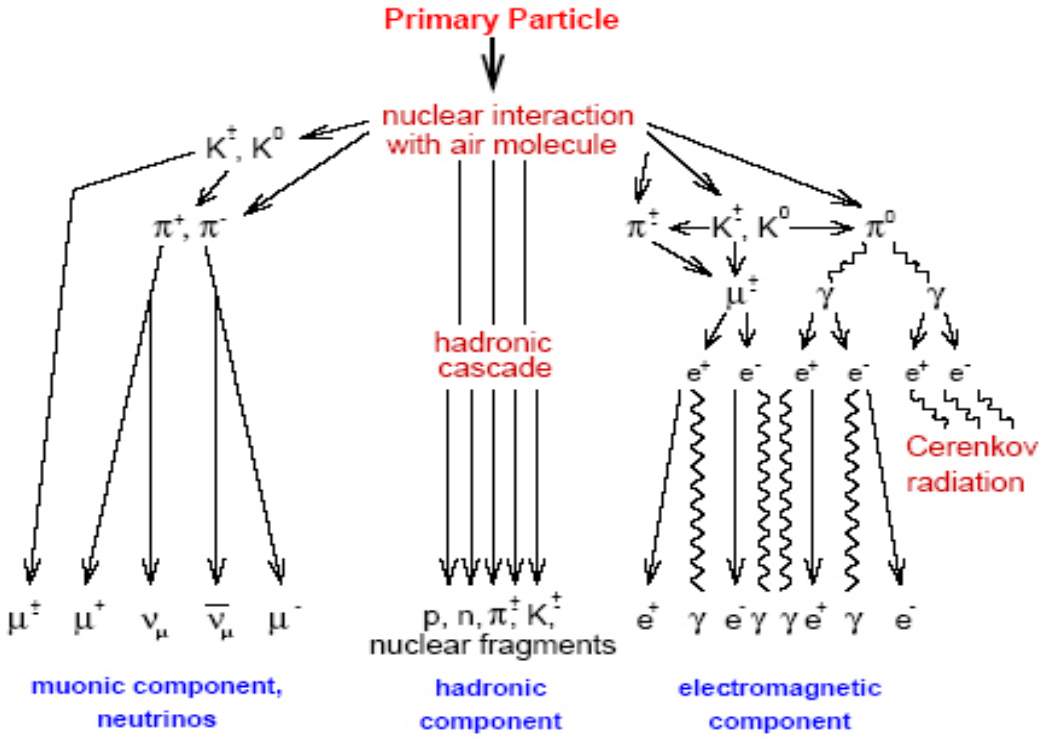

Figure 3. Schematic illustration of the development of an extensive air shower.

1.2 The PAO, a hybrid detector

Very high energy cosmic rays are detected from the extensive air showers which they produce in the atmosphere. There exist two main methods of detection, one consisting in sampling the particle density on ground and the other in detecting the fluorescence light produced on nitrogen molecules along the shower [13]. These methods have been used, or are being used, by several experiments such as Volcano Ranch, Haverah Park and AGASA for the surface detector arrays, and Fly's Eye and HiRes for fluorescence detectors. In both cases an accurate measurement of the arrival time of the measured signals makes it possible to measure the direction in the sky from which the primary cosmic ray is reaching us. But the two methods are otherwise very different: fluorescence detectors measure the longitudinal profile of the shower development, the integral of which is a direct measure of the energy [14]. Surface detectors measure instead the transverse profile of the shower at that particular stage of its development that it happens to be in when reaching ground. Its lateral extension also provides a measure of the shower energy, however much less direct than in the fluorescence case. But the fluorescence measurement is significantly more difficult than sampling on ground and its duty cycle is only 10% as it can only be made during moonless clear nights. As a result, both methods are of comparable value. Yet, as the systematic uncertainties contributing to them are so different, the value of being able to use both of them simultaneously, as is the case in the PAO, is an invaluable asset.

The PAO was therefore designed as a hybrid detector with the ability to reach the highest energies, 10^{11} GeV, with a good statistical significance. It is under current completion in the Argentina pampas and can explore the whole austral sky, including the centre of the Milky Way.

1.2.1 Longitudinal shower profile, fluorescence detector

The first fluorescence detectors were two fly's eyes [15] that were operated in Utah between 1981 and 1992. Together, they consisted of some hundred mirrors looking at the whole sky and focusing light on arrays of photomultiplier tubes, over a thousand in total. The experience gained in this pioneering work made it possible to design optimally its successors: HiRes [16] and the PAO [13]. While HiRes consists again of two fly's eyes, separated by a distance of 12.5 km, the PAO eyes (Figure 4) match the configuration of the surface detector array in order to optimize the efficiency of hybrid detection: four stations of six eyes each are located on the periphery of the array.

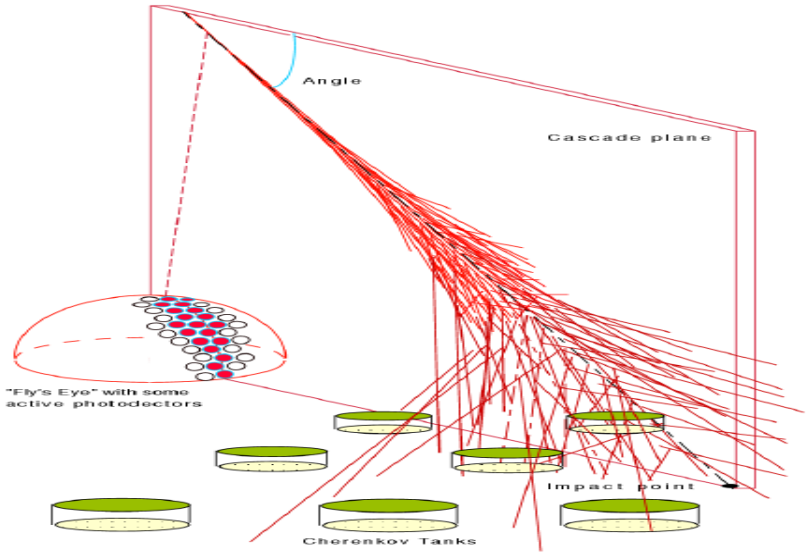

Figure 4. Schematic illustration of the hybrid concept of the PAO.

Each eye (Figure 5) covers a field of view of approximately $28^o \times 30^o$, from 62^o to 90^o in zenith angle and 180^o in azimuth for each station. It includes a UV filter and shutter to protect the detector, a 3.5×3.5 m^2 spherical mirror and an array of 440 photomultiplier tubes at its focus. The phototubes have hexagonal photocathodes closely packed together and special light guides allowing for negligible light loss at their junctions. Each phototube (pixel) has a field of view of approximately $1.4^o \times 1.4^o$ and its signal is recorded in a fast analogue to digital converter in 100 ns slices. Additional equipment is used to measure and monitor the light attenuation in the atmosphere (the attenuation length is of the order of 15 km) and to calibrate and monitor the light collection efficiency of the detector. Figure 6 shows an example of a pixel pattern observed by two neighbour eyes as well as the shower geometry.

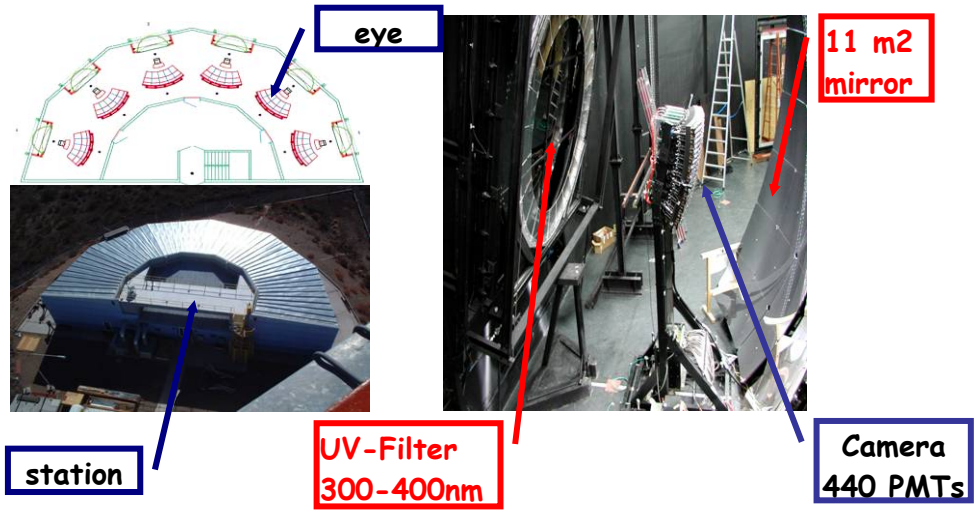

Figure 5. Auger Fluorescence Detector.

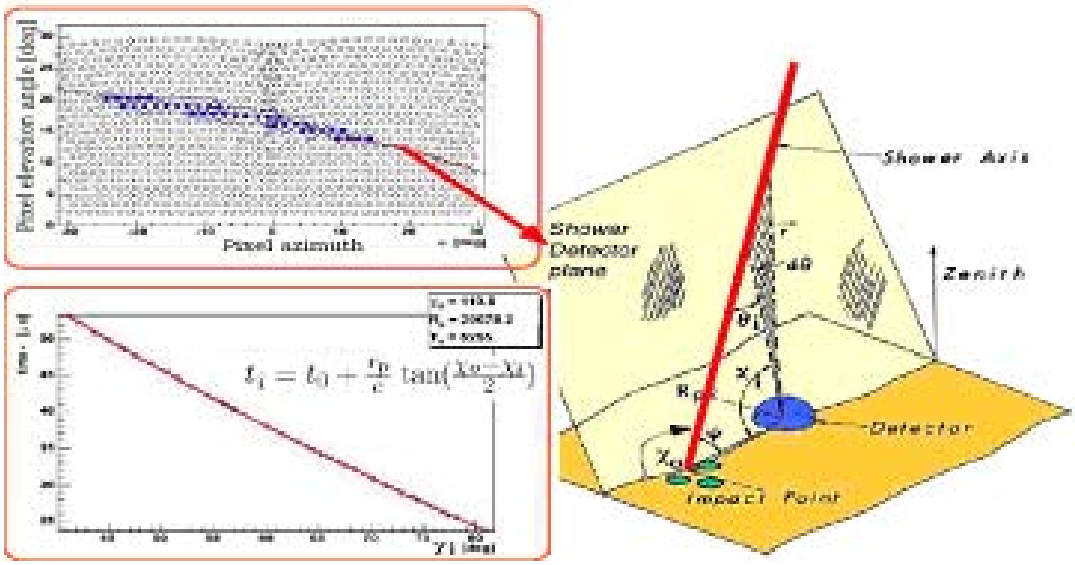

Figure 6. On the left, the upper panel shows an example of pixel patterns observed in two successive eyes. In the lower panel, the measured pixel time is plotted as a function of observed angles. On the right, the picture shows the shower geometry.

On average, the longitudinal profile of a shower induced by a given primary cosmic ray is a universal function of the depth of atmosphere traversed. It measures the total number of charged particles crossing a plane transverse to the shower axis at distance X (measured in g/cm^2) and is well described by a Gaisser Hillas function [17].

$$S(X) = S_{\max}\left(\frac{X - X_1}{X_{\max} - X_1}\right)^{(X_{\max} - X_1)/w} e^{(X_{\max} - X)/w} \qquad (1.1)$$

where $S(X)$, X_1, S_{max}, X_{max} and w are the shower size at depth X, the depth of the first interaction, the maximum value of $S(X)$, the depth at which this maximum is reached and a quantity close to the interaction length for the primary particle, usually taken equal to 70 g/cm^2, respectively. On average, while $X_{max} - X_1$ depends only on energy, X_1 depends also on the nature of the primary and X_{max} increases logarithmically with energy [18]:

$$X_{max}\,[GeV] = 107\,[g/cm^2] + 67[\,g/cm^2] \times \log_{10}E \qquad (1.2)$$

The dependence of X_{max} on energy is illustrated in Figure 7. Several factors contribute to the quality of the measurement, to its reliability and to its precision [14,15]: the air fluorescence efficiency, the subtraction of direct and scattered Cherenkov light, the attenuation and scattering of photons, and uncertainties in the geometrical reconstruction.

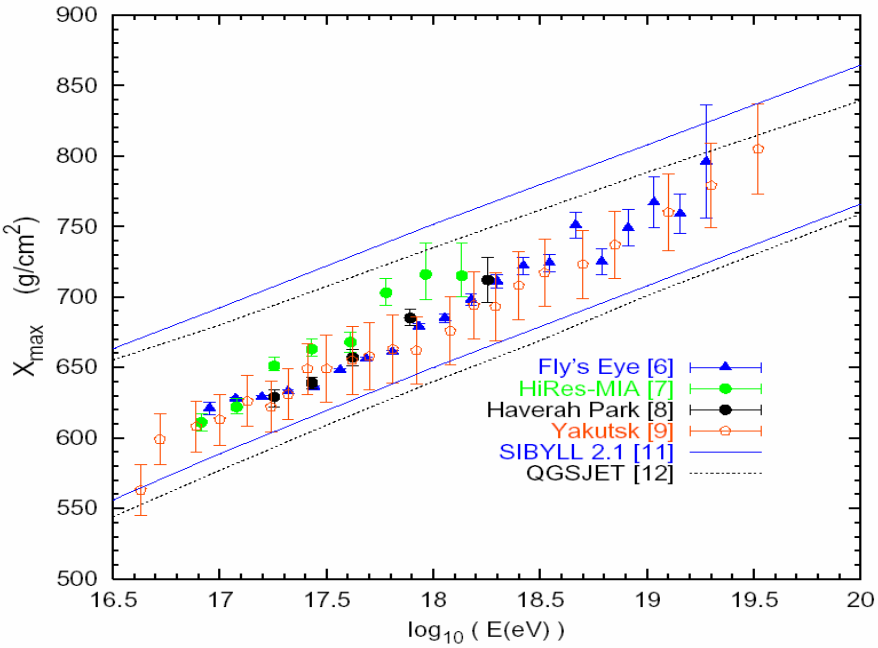

Figure 7. The correlation between X_{max} and $\log_{10}E$, E being the energy of the primary cosmic ray, as obtained from various experiments and simulations.

1.2.2 Transverse shower profile, surface detector

Both plastic scintillators and water Cherenkov counters have been used efficiently in the ground detection of showers. They behave differently. Scintillators respond to all charged particles in proportion to their energy loss in the medium while Cherenkov counters respond to charged particles having a β in excess of $1/n$, n being the refraction index of the radiator, 4/3 in the case of water. The number of photons produced by a minimum ionizing particle is of the order 20000 photons/cm in comparison with some 200 photons/cm in a water Cherenkov counter [19]. A major difference between scintillators and Cherenkov counters is the ability of the latter to convert nearly all photons, as the radiation length is of the order of 40 cm in both materials: a typical scintillator radiator is a few percent of a radiation length thick while a typical Cherenkov radiator is several radiation lengths thick. Indeed, as scintillators are expensive, they are usually made in the form of relatively thin plates (a few centimetres) that offer a cross-section to the shower that is proportional to the cosine of the zenith angle. The water Cherenkov detectors are much cheaper and can have instead a shape having similar dimensions in height and lateral extension, thereby offering to the shower a cross-section that is nearly independent of zenith angle. In practice a water depth of one meter or so is easy to implement and gives as much light as a one centimetre thick scintillator plate in the case of a minimum ionizing particle.

Cherenkov counters, which have been selected for the Auger surface detector for their lower price and good performance, are therefore very efficient detectors of soft electromagnetic showers which make up a large fraction of their signal.

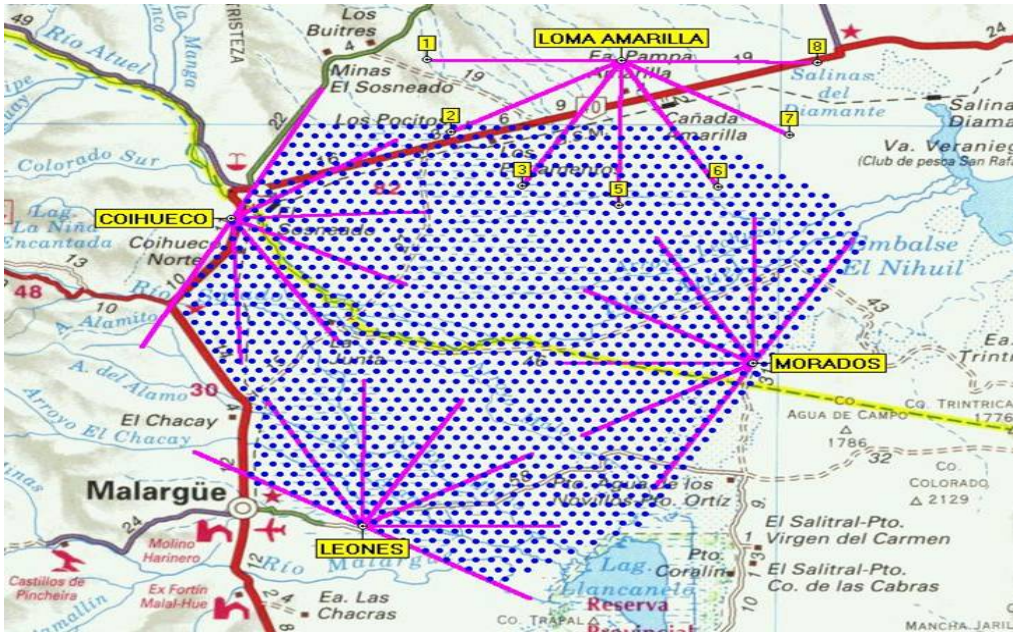

Figure 8. Map of the PAO site. Each dot represents the position of a Cherenkov tank. The array is viewed from four sides by fluorescence detectors.

The PAO surface detector (Figure 8) includes 1600 cylindrical water Cherenkov tanks covering an area of 3000 km^2. They are located at the vertices of a triangular lattice having a mesh size of 1.5 km (closest distance between two counters). Each tank (Figure 9) contains a volume of 1.2 m×10 m^2 of high purity water. The Cherenkov light produced by fast shower particles crossing the water is detected by three 9'' photomultipliers. Their signals are recorded, in 25 ns bins, in flash analog to digital converters (FADC's) equipping both the anode and last dynode. A reasonably low threshold is used, well below the signal given by relativistic minimum ionizing particles.

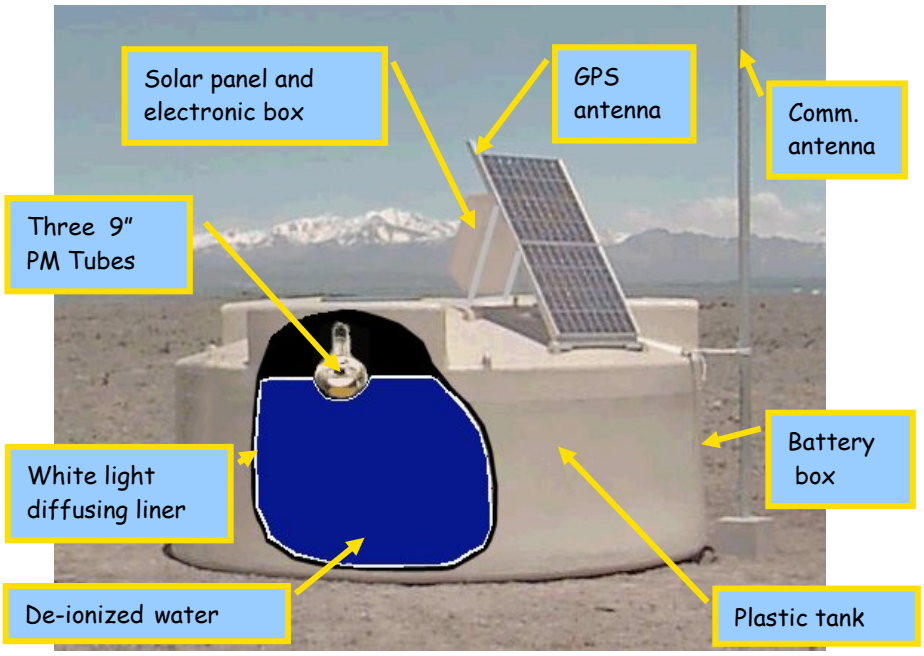

Figure 9. Exploded view of an Auger Cherenkov tank.

1.2.3 Lateral distribution function

In the 10^{11} GeV region, each shower typically involves 15 to 20 detectors and occurs at a rate of one per month or so. A fit of the tank signals to a lateral distribution function (LDF) that relates the signal amplitude S to r (its distance to the shower axis) and E (the shower energy) is made for each event. In Auger, the LDF is taken of the form $S(r[km])=S(1000)\ r^{-\nu}$ with $\nu= 4.8–1.26\ sec\theta$ and the shower energy is inferred from the relation $E(EeV)=0.12(\sqrt{\{1+11.8(sec\theta -1)^2\}}\ S(1000))^{1.05}$ [13]. The angular and energy resolutions of the ground array have been estimated from simulations of the detector to be ± 1.5° and ± 20% respectively.

In the Ha Noi experiment, we are dealing with much lower energy showers which, rather than being at maximum development, are nearing the tail. The Kascade array [20], in Germany, has devoted much effort to a detailed study of the LDF of showers in the knee region. As an example, Figure 10 shows their result in the case of low energy muons (>2GeV). A steep slope, on a scale of 10m, applies to the core while a much larger scale, around some 100 m, applies to the tail. In the geometry of the Ha Noi experiment, it is of course the shorter of these two scales that is expected to describe the data.

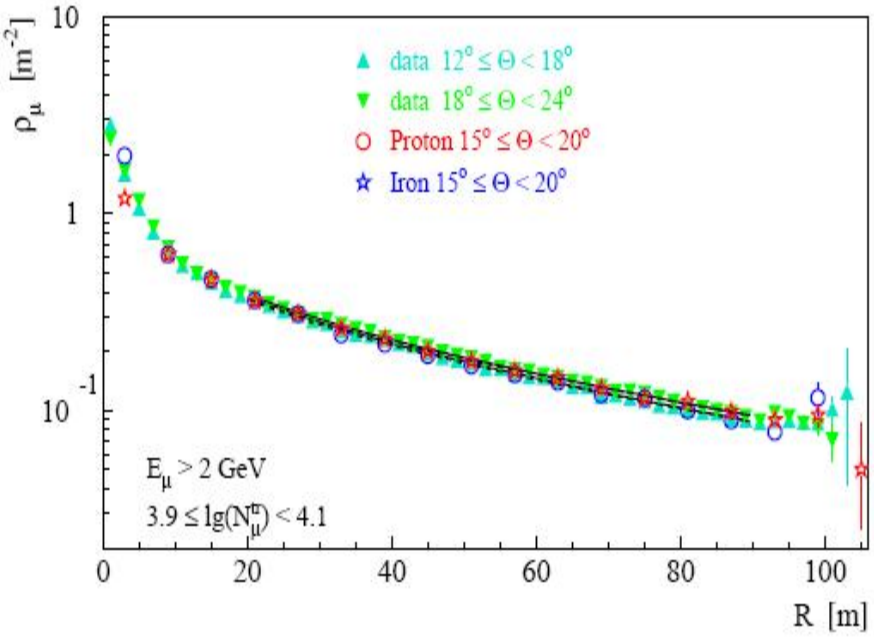

Figure 10. The lateral distribution function measured in Kascade for low energy muons.

2. THE HANOI EXPERIMENT

A set of four Cherenkov counters has been installed on top of the roof of the VATLY laboratory in Ha Noi.

One of these is a copy of a PAO tank and has been described and studied in several places [1, 2]. It contains a cylindrical volume of pure water, 3.6 m in diameter and 1.2 m in height, seen by three 9" photomultiplier tubes (PMT).

Three smaller counters surround it with the aim of serving as a trigger for extensive air showers that would then be likely to include particles entering the main counter. They are described in detail below.

2.1. A trigger on extensive air showers: general strategy

In order to have as little trigger bias as possible, the idea was to only require a two-tank coincidence in the trigger and to leave the requirement of a three-tank coincidence for the off-line analysis. Indeed the two-tank coincidence rate is of the order of 0.5 Hz and the three-tank coincidence rate is of the order of 0.1Hz, making this trigger strategy very sensible.

The use of three tanks allows in principle to measure the direction of arrival of

the shower, implying that the time of arrival of each of the tank signals is accurately measured. Moreover a charge measurement of each of the tank signals is desirable in order to study correlations with the size of the signal measured in the main tank. It was decided to equip each tank with a pair of phototubes, a minimum requirement to suppress thermal noise. While the time difference between the two signals of a same tank is small, allowance must be made in the coincidence electronics for larger time differences between the signals of different tanks, corresponding to large zenith angles and/or excentric impacts.

2.2 The water tanks

The tanks are 3000 litres standard water tanks, each being equipped with two upper holes used to house the PMTs. They are horizontal cylinders with a length of 170 cm and a diameter of 145 cm. They are made of stainless steel and the inner surface quality was considered sufficiently good to use it as such, namely without any additional coating. They were filled with filtered water that was previously contained in the main tank where iron oxide dust had time to settle down for nearly two years. The exact location of the tanks is shown in Figure 11.

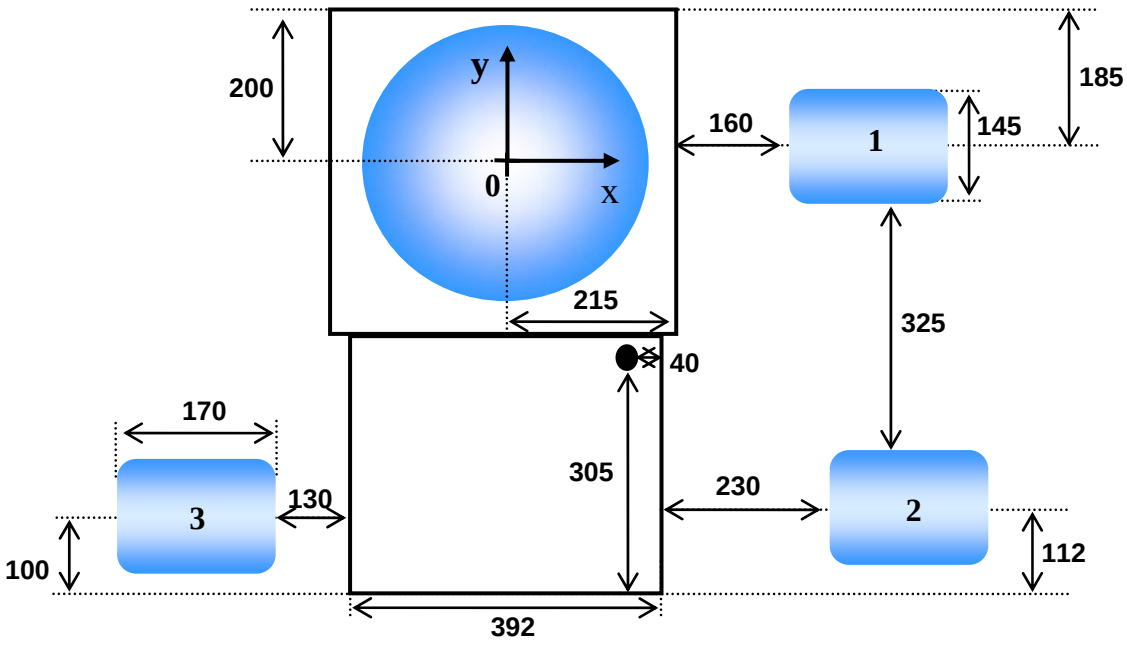

Figure 11. Plan view of the VATLY Cherenkov counters including three small (3000 l) tanks used as a trigger and a large (12000 l) main tank. All distances are measured in cm.

2.3 The phototubes

The phototubes are EMI D340A eleven dynodes phototubes having a spherical photocathode of 8" diameter. As they are over 30 years old, their photocathode efficiency has deteriorated to something like 10%. In order to cope with the relatively low number of collected photoelectrons, each signal is amplified by a factor 10. A typical track length of 1 m corresponds to some 20000 Cherenkov photons in the case of a relativistic particle. The ratio between the photocathode area and the inner walls area is 0.6%. For a single diffusion, assuming perfect randomization and no loss, we have therefore 20000×0.006×10%=12 photoelectrons. The quality of the water transparency and of the wall diffuseness do not allow for more than one effective diffusion. The duration of the light pulse should not exceed 10 or so nanoseconds corresponding to a 2m light path in water where the light velocity is 20cm/ns.

In order to avoid microsparking across the glass of the phototube envelope, the photocathode, immersed in water (Figure 12), is grounded while the anode is biased at some +2kV: the signal is read out across a 10^4 pF capacitor.

The signal cable (50 Ω coaxial) and high voltage cable associated with each PMT are enclosed into light tight PVC tubes that end in the central cabin that communicates with the laboratory through a hole in the roof. While the signal cables go directly to the laboratory, the high voltage cables go to a distribution panel in the central cabin. This panel is fed with only three independent high voltage cables that split into two: this way we can use a single high voltage supply for two phototubes having similar gains.

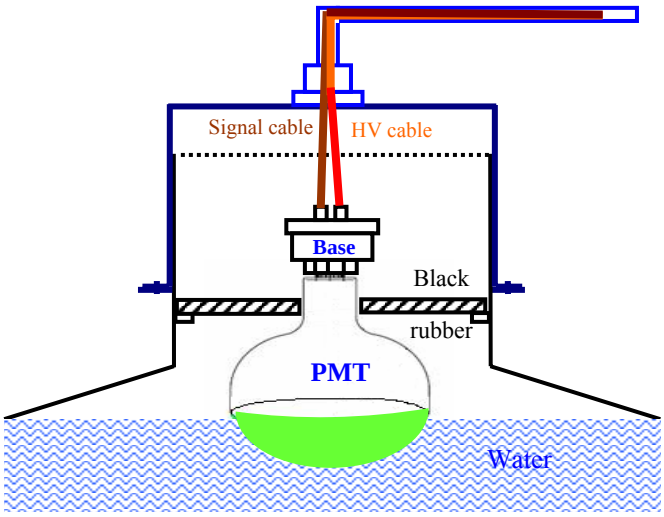

Figure 12. Holding system of PMT in the small Cherenkov tanks.

2.4 Electronics

Each PMT signal, after amplification, is resistively split into two equal pulses. One of these is sent after some delay to an analog-to-digital converter (ADC) for measuring its charge. The other is sent to a fast discriminator that produces a NIM pulse used for building up the trigger and, after some delay, for stopping the time to digital converters (TDC) that are started by the trigger pulse.

A schematic drawing of the trigger electronics is shown in Figure 13. Three fourfold coincidences are used to build the three possible two-tank coincidences, requiring each time a coincidence of the four phototube signals implied. The discriminator threshold and width were set at 4 mV and 40 ns respectively. An OR of the three two-tank coincidences makes the final trigger. While the timing of each two-tank coincidence is defined by the latest of the four pulses contributing to it, the timing of the main trigger is instead defined by the earliest of the two-tank signals contributing to it.

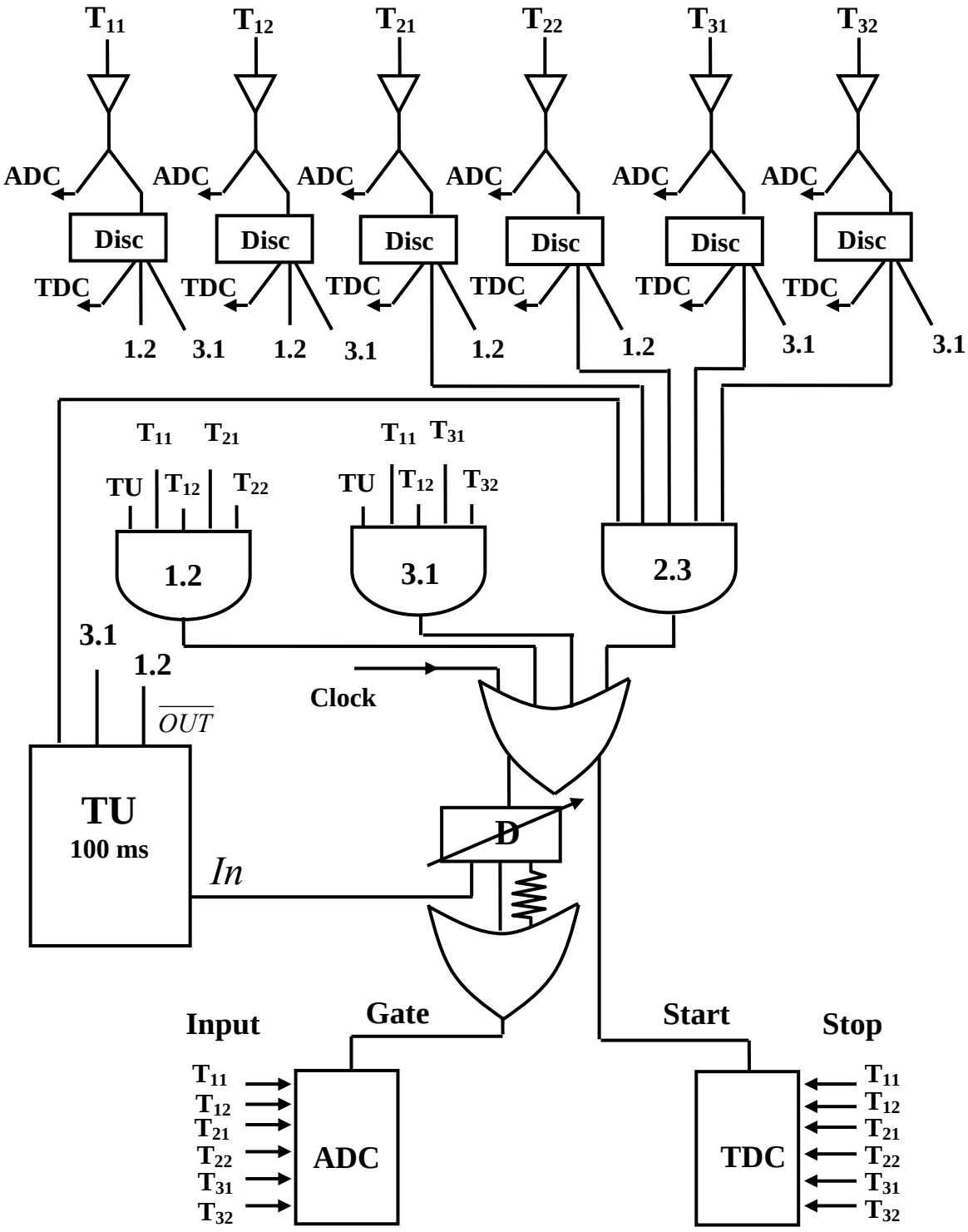

Figure 13. Electronics diagram of the trigger logic.

2.5 Data acquisition

The data are collected into CAMAC units that are read out into the data acquisition PC using a CAMAC controller. The CAMAC units are a 12 input ADC LRS 2249A, a 8 input TDC LRS 2228A, and a 16 bit scaler of a four-scaler unit RRC 4CH 80MHz. The scaler records the output of a 10 kHz clock in order to measure the time separating successive triggers, and therefore the trigger rate (the distribution of this quantity is expected to be exponential with both the mean and rms values equal to the reciprocal of the rate). All units are reset at each trigger by a software command. The readout operation is started by sending an appropriate signal (LAM=look at me) to the CAMAC controller whenever the ADC receives a gate, again using a software command.

3. SIMULATION OF THE DETECTOR

3.1 General strategy

Our aim is to understand the events which satisfy the triple coincidence requirement: they provide the trigger for the study of the main Cherenkov tank.

Some preliminary remarks will help the following discussion. From our earlier study of the muon flux [21,22], we know that most muons were usually isolated and represented the main fraction (92%) of the cosmic flux. The reason is that Ha Noi is located at sea level and the atmosphere thickness represents 11 interaction lengths. As the primary flux decreases with energy approximately as $E^{-2.7}$ the fraction having an energy smaller than ε is $\frac{\int_{17}^{\varepsilon} E^{-2.7} dE}{\int_{17}^{\infty} E^{-2.7} dE} = 1 - \left(\frac{\varepsilon}{17}\right)^{-1.7}$: 90% of the primary flux has energies below 66 GeV. Here the integration is made from 17 GeV onwards, assuming a sharp rigidity cut-off (in practice, the cut-off is smeared and our evaluation is underestimated). Showers of such energy reach their maximum around five interaction lengths and are well beyond maximum development when they reach ground: at sea level we can only see their tails. Evidence for this was also obtained from the study of the dependence of the flux on ambient temperature and pressure [23]. The situation is much worse for inclined showers, for which the thickness of the atmosphere traversed increases as $1/\cos\theta$ where θ is the zenith angle. In the case of muons, the atmosphere thickness is of much lesser relevance because of their much higher penetration and the flux extends over large zenith angles. But the triple coincidence trigger should select

events of a very different nature: the shower cannot have developed too far on its tail. This means that we can expect a much steeper angular distribution than in the muon case, inclined showers being unable to make it through the thicker atmosphere.

Accordingly we may expect a significantly lower rate than obtained for muon events. The steepness of the energy spectrum implies that most showers that satisfy the triple coincidence trigger will be concentrated in energy near some effective threshold resulting from the competition between the rate of decrease (and the fluctuations) of the longitudinal shower profile and that of the energy spectrum. This feature should make it possible to describe the shower events on average, with a limited number of parameters. In practice we shall use a three parameter model: one for the angular distribution, one for the particle density in the shower and one for the lateral distribution function (the latter two being of course on ground, namely at sea level).

The first parameter, a_θ, defines the width of the zenith angle distribution. The flux per unit of solid angle is taken to be Gaussian, of the form $exp\{-1/2(\theta/ a_\theta)^2\}$. This choice is adequate because the angular acceptance of the detector is broad and the observed zenith angle distribution is steep. Moreover, as we shall see, the uncertainty attached to the measurement of the zenith angle is large. This is illustrated in Figures 14, 15 and 16 for triple coincidences with a charge cut of 10 ADC channels[1], where the Monte Carlo simulation described below has been used to evaluate the angular acceptance (of the order of 30 m^2).

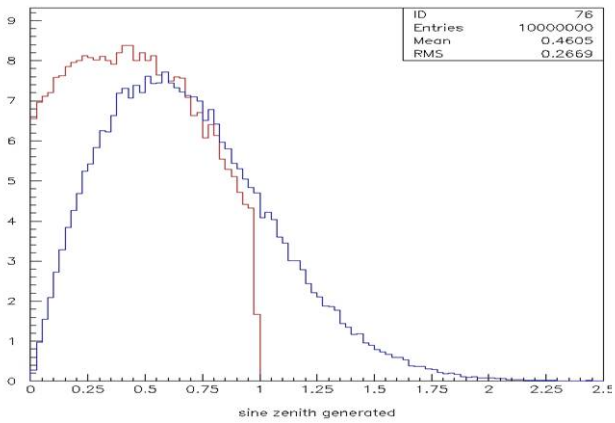

Figure 14. Generating showers with a Gaussian θ distribution (a_θ=0.57 rd) gives the narrower sinθ distribution (in red) for three tank coincidences. The distribution of the reconstructed value of sinθ is significantly smeared (in blue).

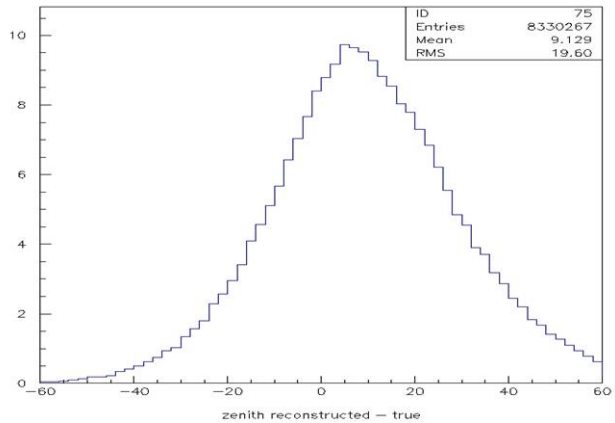

Figure 15. Distribution of the difference between the reconstructed and generated values of the zenith angle (in degrees) for showers generated with a Gaussian θ distribution (a_θ = 0.57 rd).

[1] The charge cut applies to the small tank signals and is introduced in the next section.

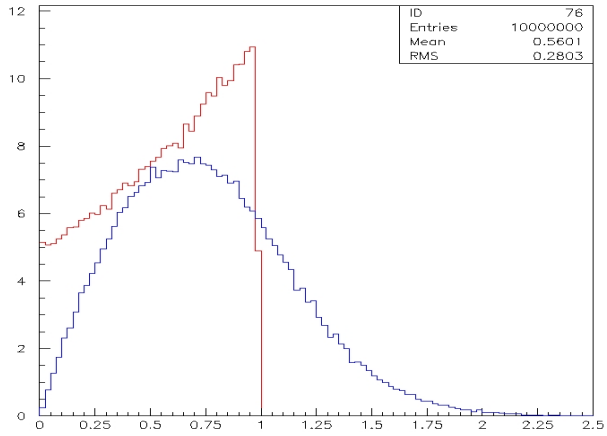

Figure 16. Acceptance of the detector as a function of sinθ. Showers are generated with a uniform distribution in sinθ. The sinθ distribution of showers giving a three tank coincidence is given by the sharply peaking (red) curve, it is the detector acceptance (in m^2 per bin). The other (blue) curve is the distribution of the reconstructed value of sinθ, smeared by measurement errors.

As the observed width of the zenith angle distribution (~19^o) does not much exceed the smearing due to measurement uncertainties (~10^o), it is not possible to measure accurately the real distribution and a Gaussian approximation is therefore sufficient.

The second and third parameters describe the particle density at sea level in a plane normal to the shower axis. The total number of particles, m, is taken to have a Poisson distribution with mean m_0. In practice, we shall find that large values of m_0 are required to describe the data. Typically, m_0 will be of the order of 150. The corresponding particle densities are of the order of 5 particles per square meter in the core. In practice, for such high multiplicities, the Poisson distribution can be replaced by a Gaussian distribution. The last parameter, ρ_0, describes the lateral distribution function, namely the dependence of the particle density on the distance to the shower axis which is taken of the form $exp(-\rho/\rho_0)$. It takes values between 2 and 2.5 metres.

In practice, it will be easy to adjust these three parameters because we can find quantities on which their effects are weak. The zenith angle distribution fixes a_θ, the ratio of double to triple coincidences nearly fixes the value of m_0 and the ratio of 1-2 coincidences to double coincidences is very sensitive to the value of ρ_0. The latter is because tanks 1 and 2 are more than a factor two closer to each other than 1 and 3 are.

The importance of the Monte Carlo simulation and of this simple three-parameter model is obvious: it will make it possible for us to compare observations and predictions, namely to understand the properties of the shower sample on which we trigger, and to predict which signal should be expected in the main Cherenkov

tank. A simple Monte Carlo program has therefore been written in this spirit with the aim to simulate the main features of the detector.

3.2 Geometry

It uses coordinates (Figure 17) such that *x* points to the west, *y* to the south and *z* up. The unit vectors along *Ox*, *Oy* and *Oz* are called ***i***, ***j*** and ***k.*** The coordinates of the centre of each tank are listed in Table 1.

Table 1*: Coordinates of the tank centres* C_i

	1	*2*	*3*	*4*
x_i*(cm)*	*460*	*511*	*−411*	*0*
y_i*(cm)*	*15*	*−448*	*−460*	*0*
z_i*(cm)*	*26.3*	*31.5*	*25.5*	*60*

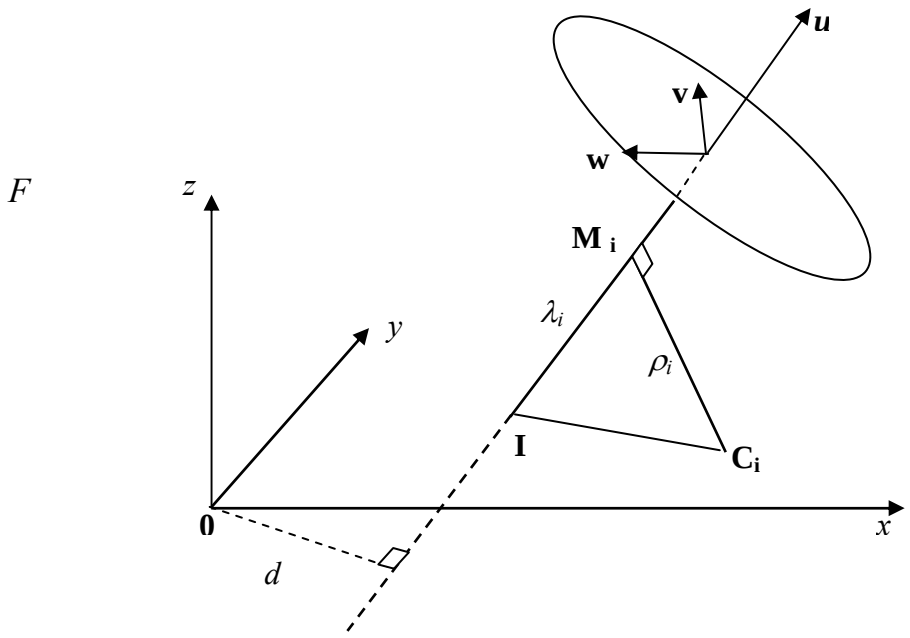

Figure 17. Definition of the parameters used to describe an air shower. The shower axis (unit vector ***u****) impacts ground in I and one counter (*C_i*) measures a signal* s_i *at time* $t_i = -\lambda_i$.

We call *I* the impact on the laboratory roof ($z = 0$) of the shower axis, x_{imp} and y_{imp} its coordinates, ***u*** the unit vector directed along the shower axis (the cosmic ray flies along $-\boldsymbol{u}$), $\boldsymbol{C_i} = (x_i, y_i, z_i)$ the coordinates of the centre of counter *i* (*i*=1 to 4), M_i

the projection of $\boldsymbol{C_i}$ on the shower axis, θ and φ the zenith angle and azimuth of vector $\boldsymbol{u}$, ρ_i the distance from $\boldsymbol{C_i}$ to the shower axis. We have:

$$\rho_i^2 = IC_i^2 - \lambda_i^2 = (x_{imp} - x_i)^2 + (y_{imp} - y_i)^2 + z_i^2 - \lambda_i^2 \qquad (3.1)$$

where $\lambda_i = (\boldsymbol{C_i} - \boldsymbol{I}).\boldsymbol{u} = (x_i - x_{imp})\sin\theta\cos\varphi + (y_i - y_{imp})\sin\theta\sin\varphi + z_i\cos\theta \qquad (3.2)$

In the approximation of a planar shower front, and defining $t_0 = 0$ the time at which the shower front hits point I, the time t_i at which it hits counter C_i is :

$t_i = -\lambda_i$.

We call d the distance of the shower axis to the origin of coordinates.

3.3 The simulation algorithm

The simulation starts with the generation of a shower axis having a distribution uniform in azimuth φ (from -180^o to 180^o) and Gaussian in zenith angle θ (with rms a_θ). We ignore the east-west asymmetry of the primaries resulting from the effect of the Earth magnetic field as it is small, at most a percent in the present range of zenith angles, and as the azimuth is anyhow very poorly measured. We generate shower axes at distance d from the origin with a uniform density within the cylinder $d < d_{max}$. We define two unit vectors, $\boldsymbol{v}$ and $\boldsymbol{w}$, such that $\boldsymbol{uvw}$ is an orthonormal system and

$\boldsymbol{v} = \boldsymbol{i}\times\boldsymbol{u} / |\boldsymbol{i}\times\boldsymbol{u}|$ and $\boldsymbol{w} = \boldsymbol{u}\times\boldsymbol{v}$.

We call ψ the azimuth angle of a vector in the $\boldsymbol{uvw}$ system. ψ and d^2 are generated with uniform distributions (between 0 and 2π and between 0 and d_{max}^2 respectively). To each shower we assign a given weight W that is the product of various factors described below.

As was said above, we define the shower profile by two parameters, m_0 and ρ_0. The lateral distribution function, which measures the particle density in a plane transverse to the shower axis, is taken of the form $dN / (\rho\, d\rho\, d\psi) = I_0 \exp(-\rho/\rho_0)$ with $I_0 = m / (2\pi\rho_0^2)$, such that its integral over the plane is equal to m. This is the distribution of particles, or sets of particles, that give a signal above threshold in the single tanks and ρ is the distance to the shower axis. Both m_0 and ρ_0 will be varied in order to make the measured data agree with the prediction of the simulation.

Having generated a shower axis in space, we define the shower multiplicity m according to a Poisson distribution of mean m_0. We then calculate, for the centre of each of the three tanks, the quantity $\varepsilon_i = \exp(-\rho_i/\rho_0)$. The mean value of the number

of particles hitting tank i is proportional to $m\varepsilon_i$, it is in fact equal to $w_{1,i}=m\varepsilon_i S_\zeta/(2\pi p_0^2)$. Here, S_ζ is the tank cross section seen by the shower, the same for each of the three tanks since they have their axes parallel to each other. The cross section of a horizontal cylindrical tank having diameter D and length L is $S_\zeta=D\,(\pi D\cos\zeta/4+L\sin\zeta)$ where ζ is the angle between the cylinder and shower axes, $\cos\zeta=\sin\theta\cos\varphi$ where $\varphi=0$ is taken along the axis of the cylinder. The dependence of S_ζ on ζ is shown in Figure 18.

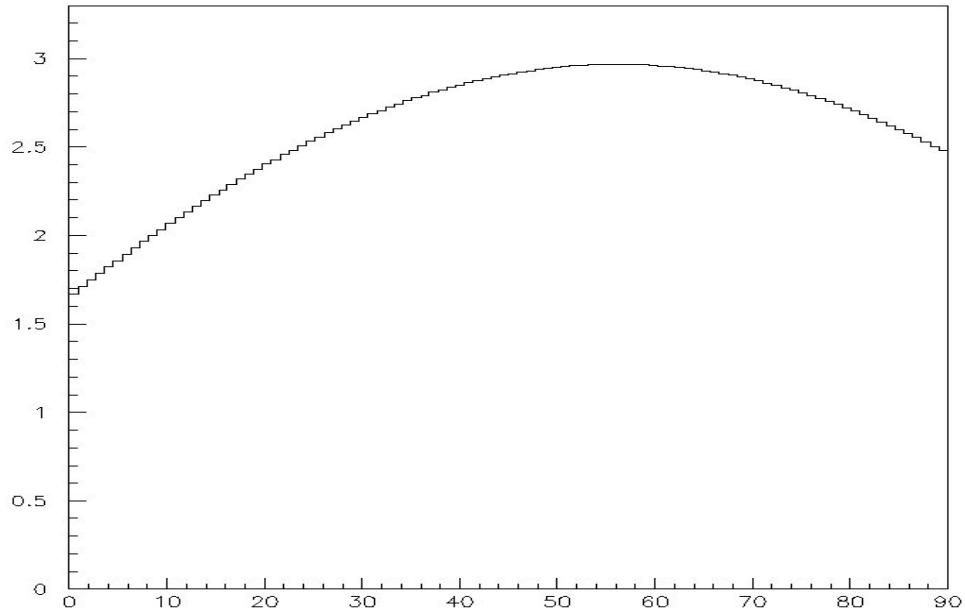

Figure 18. Cross-section of a small tank (in m^2) as a function of the angle ζ (^{o}) between the tank and shower axes.

The probability for tank i to be missed is $\exp(-w_{1,i})$, namely the value at zero of a Poisson distribution with mean $w_{1,i}$. The probability for tank i to be hit is therefore $1-\exp(-w_{1,i})$. Accordingly, we give each tank a weight

$W=(1-\exp(-w_{1,i}))\pi d_{max}^2/N_{gen}$ where N_{gen} is the number of generated showers (because we generate N_{gen} showers per πd_{max}^2). Similarly, the probability that the shower hits tanks i and $j\neq i$ but not tank $k\neq i,j$ is:

$$w_{2,ij}=(1-\exp(-w_{1,i}))(1-\exp(-w_{1,j}))\exp(-w_{1,k})$$

and we give each pair (i-j=1-2, 2-3 or 3-1) a weight $W=w_{2,ij}\pi d_{max}^2/N_{gen}$.

Similarly again we give a weight $W=w_3\pi d_{max}^2/N_{gen}$ to the triple coincidence trigger with $w_3=(1-\exp(-w_{1,i}))\,(1-\exp(-w_{1,j}))\,(1-\exp(-w_{1,k}))$. In so doing, we neglect correlations between the three tanks, a reasonable assumption as m_0 is large and $m(m-1)$ or $m(m-1)(m-2)$ are nearly equal to m^2 and m^3 respectively.

The double rates defined this way are exclusive rates, namely they exclude the triple rates.

With our definition of the weights, they measure the acceptance of the detector for the process being considered in square meters (assuming that d is measured in meters), integrated over solid angle for the Gaussian θ distribution having variance a_θ.

Namely the measured flux of showers, integrated over solid angle, is the observed rate divided by the proper weight. The acceptance of the detector for singles (exclusive), for double (exclusive) coincidences and for triple coincidences, using a charge cut of 10, is summarized in the table below and its dependence on d^2 is illustrated in Figure 19. Note that the simulation code uses $d_{max}=50\ m$, which is amply sufficient.

***Table 2**: Acceptance of the detector for a 10 ADC channel cut.*

	Acceptance (m^2)	*$<d^2>$ (m^2)*	*$<d^2>^{1/2}$ (m)*
Singles	*267*	*129*	*11*
Doubles	*109*	*56*	*7.5*
Triples	*26*	*29*	*5.4*

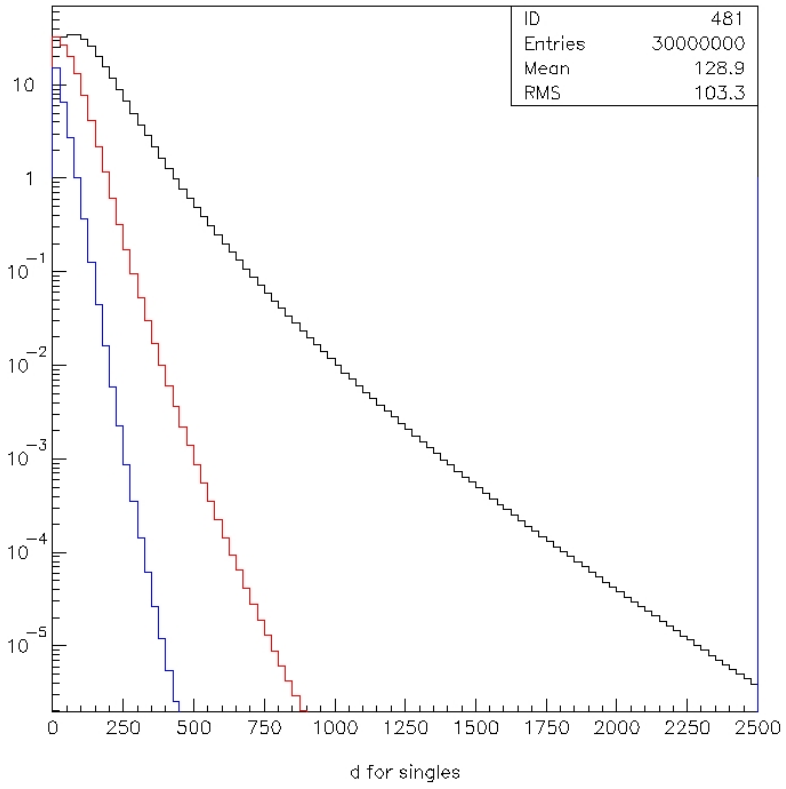

Figure 19. Dependence on d^2 of the detector acceptance for singles (black), double (red) and triple (blue) coincidences. Both d^2 and the acceptance are measured in m^2, the acceptance being integrated over energies and solid angles.

The time t_i at which a signal is recorded is given by relation (3.2). From the three tank times we can reconstruct the shower axis using this relation. In the approximation where the three z_i's are equal, and calling

$$D(a,b) = a_1(b_2 - b_3) + a_2(b_3 - b_1) + a_3(b_1 - b_2),$$

we find $\alpha = \sin\theta \cos\varphi = D(t,y)/D(x,y)$ and $\beta = \sin\theta \sin\varphi = D(t,x)/D(x,y)$, from which $\theta = Arcsin\sqrt{\alpha^2 + \beta^2}$ and $\varphi = Arctan(\beta/\alpha)$.

In the particular case where $x_1 = x_2$ and $y_2 = y_3$, which is nearly ours,

$D(t,y) = (t_3 - t_2)(y_1 - y_2)$, $D(t,x) = (t_1 - t_2)(x_1 - x_3)$ and $D(x,y) = (x_3 - x_1)(y_1 - y_2)$

namely $\alpha = (t_3 - t_2)/(x_3 - x_1)$ and $\beta = (t_1 - t_2)/(y_2 - y_1)$. (3.3)

As $(y_2 - y_1)$ is twice as small as $(x_3 - x_1)$, the uncertainty attached to the measurement of β is twice as large as that attached to the measurement of α. In the simulation we simply attach Gaussian errors to the measurements of the tank times. We discuss in the next section how they are evaluated. We use these uncertainties to smear the tank times when calculating reconstructed quantities.

4. DATA ANALYSIS AND COMPARISON WITH THE PREDICTIONS OF THE SIMULATION

4.1 Data processing

Data processing proceeds along the following steps:

4.1.1 Analog to digital converters

The pedestals of the ADCs are constantly updated according to a simple algorithm taking advantage of the fact that, in any double coincidence trigger that is not a triple coincidence, one tank is likely to have received no signal and is therefore a good candidate to evaluate its ADC pedestals. We monitor the pedestals as a function of time: the result is shown in Figure 20.

Variations of the pedestals are sometimes observed, usually associated with a change of input impedance resulting from a bad contact in one of the connectors along the line bringing the signal from the PMT to the ADC. Moreover, an important VHF pick up is present on all signals, having its source in the television and mobile phone emissions in the neighbourhood. But once they are averaged over the 160 ns fixed width ADC gate, their contribution is fortunately small enough not to disturb the quality of the charge measurements.

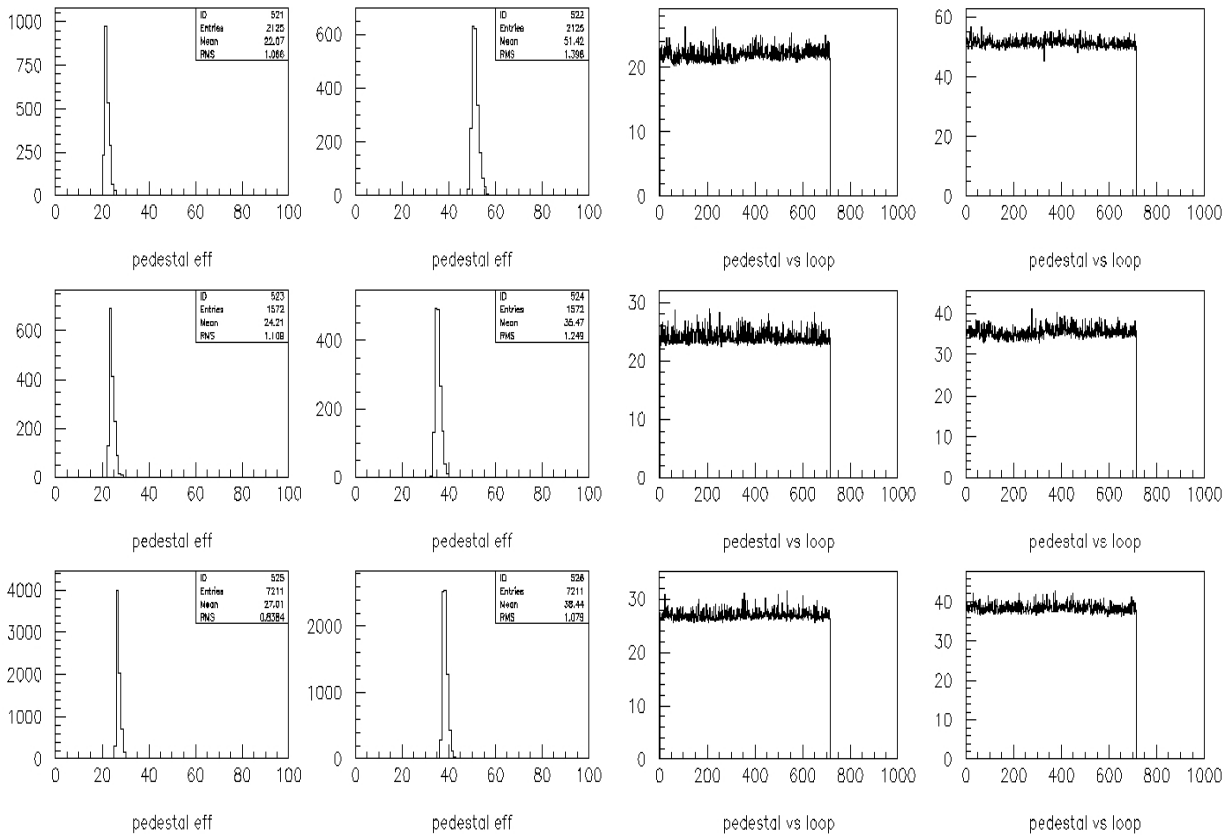

Figure 20. Pedestals of the small tanks.

The six panels on the left show the distribution of the pedestals as calculated at regular intervals over the whole data sample considered here.

The six panels on the right show their dependence on time (from the beginning to the end of the run).

Each charge is pedestal subtracted and corrected for the PMT gain in order to scale it to a standard average of 70 ADC channels. This step is necessary because of the constraint of using a same high voltage value for a pair of PMTs. The values by which each raw charge had to be divided in the data presented here were: 0.87, 1.25, 1.07, 0.63, 0.44 and 0.95 respectively. Each tank is then tagged as being "on" as long as its charge exceeds some threshold (normally 2, but in some cases 10 or 18 ADC channels) and as its time measurement is within a broad window. Figures 21 and 22 show the charge and time distributions for "on" tanks. The charges are steeply decreasing as expected: muons contribute only a minute fraction of the triggers and the tank geometry is such that their track lengths can take very different values (contrary to the case of the main Cherenkov tank). Moreover the photons, which constitute the main component of the showers on which we trigger, are quite soft and their energy is rapidly absorbed in the water. Tank charges are defined as the mean value of the PMT charges of that tank; their distributions are shown in Figure 23 for "on" tanks.

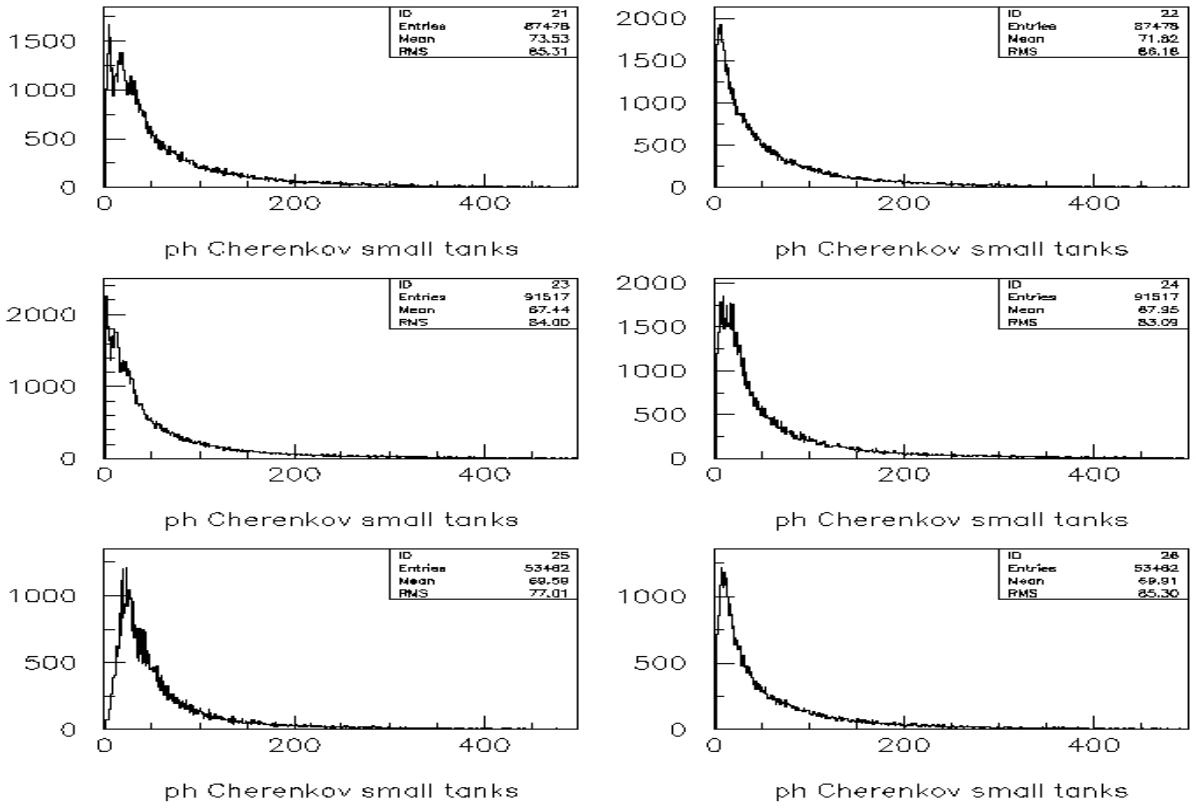

Figure 21. Small tank charge distributions for "on" tanks (2 ADC channel cut).

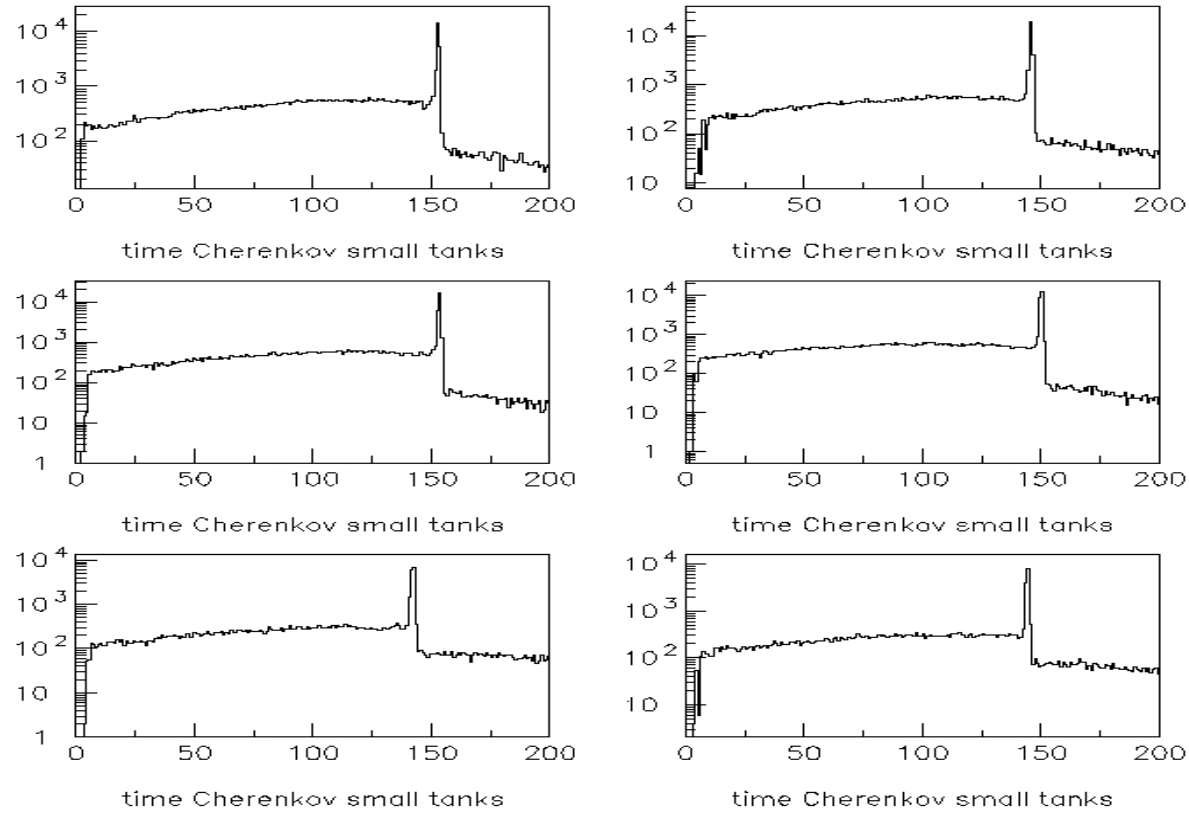

Figure 22. Small tank time distributions for "on" tanks (2 ADC channel cut).

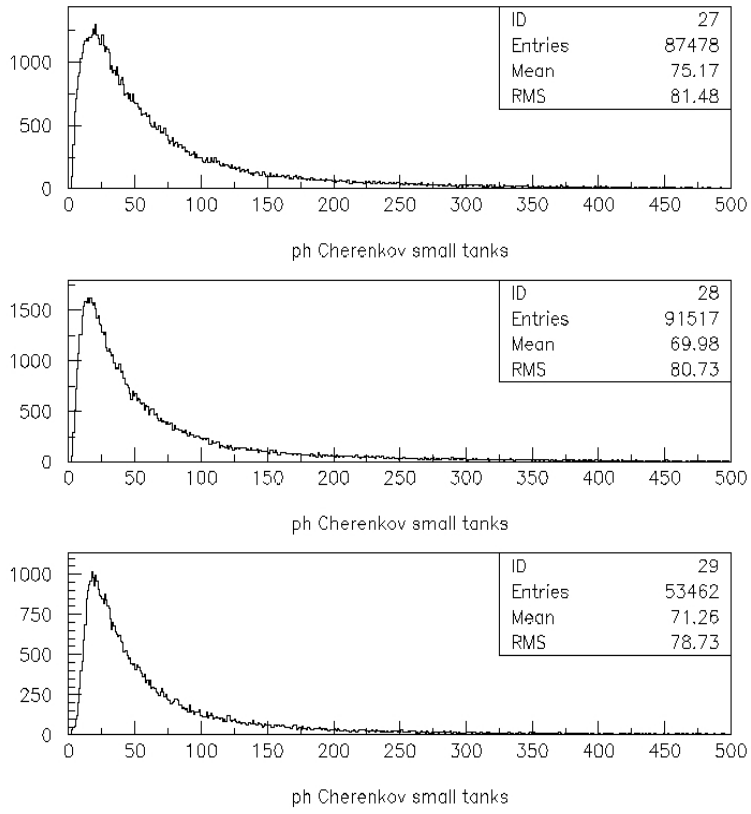

Figure 23. Tank charge distributions for "on" tanks (2 ADC channel cut).

4.1.2 Time to digital converters

The PMT time distributions (Figure 22) show a spike corresponding to cases where the PMT being looked at defines the timing of the trigger. This happens when it is the latest of the four PMTs of the pair of tanks giving a trigger coincidence. In such a case the TDC start, given by the trigger, is the same signal as the TDC stop, the value of the time measured corresponding simply to different cable lengths. The timing of a coincidence is defined by the latest of the input pulses while that of an OR is defined by the earliest. We can tell which PMT of which tank, say PMT *i* of tank *j*, has defined the timing of the trigger because its TDC value falls onto the spike of its distribution, which usually happens for only one of the six PMT's (Figure 24). The other PMT of tank *j* must arrive earlier, which it does (Figure 25), otherwise it would have defined the timing of the trigger and would have fallen on the spike of its distribution. One of the two other tanks, that which belongs to the coincidence having defined the timing of the trigger, must have both of its PMT's also arriving earlier, for the same reason, while at least one of the PMT's of the third tank must arrive later in order to ensure that the coincidence that does not include tank *j* arrives late in the OR.

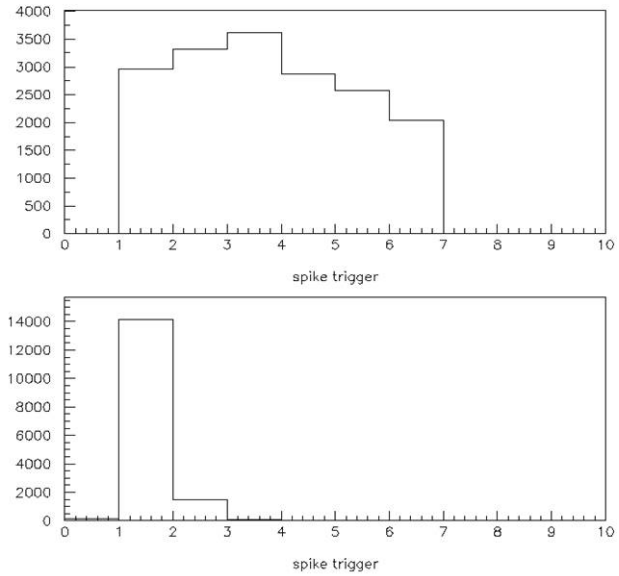

Figure 24. Timing defining PMT's (their distribution is shown on the top panel) are usually uniquely defined as falling in their spike as shown in the bottom panel.

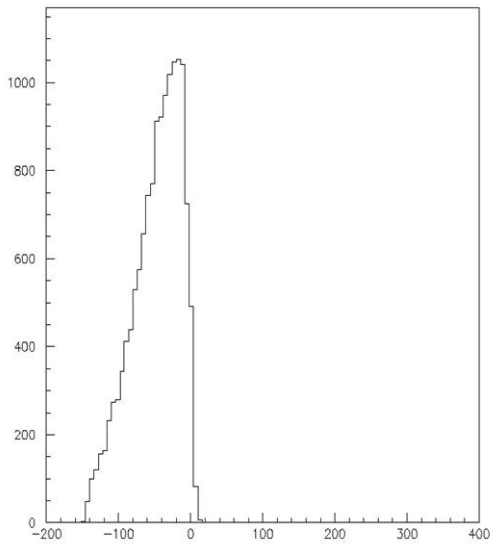

Figure 25. Time of arrival of the signal of the timing defining tank that does not define the timing.

Let us take an example: assume that the time sequence of pulses is (12) (21) (31) (11) (22) (32). The timing of the 1-2 coincidence is then defined by (22), that of the 2-3 coincidence by (32) and that of the 3-1 coincidence by (32). That of the trigger is defined by (22): (21), (11) and (12) arrive earlier and at least one of (31) and (32), in the present case it is (32), arrives later. We can therefore identify the third tank as being the tank having at least one signal arriving later than that which defines the timing of the trigger. Figure 26 (top) shows the distribution of the time of arrival of the latest signal, it is indeed always larger than the time of arrival of the signal which defines the timing of the trigger. Figure 26 (bottom) shows the time of arrival of the other PMT of this third tank, (namely both PMT's of Figures 26 belong to the same tank): as expected, it may arrive earlier or later than the signal which defines the timing of the trigger.

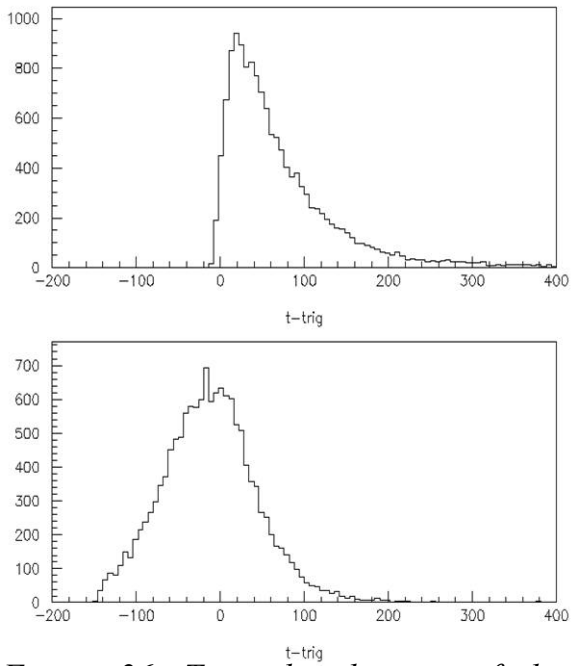

Figure 26. Time distributions of the signals of the tank that does not take part in the timing defining coincidence.

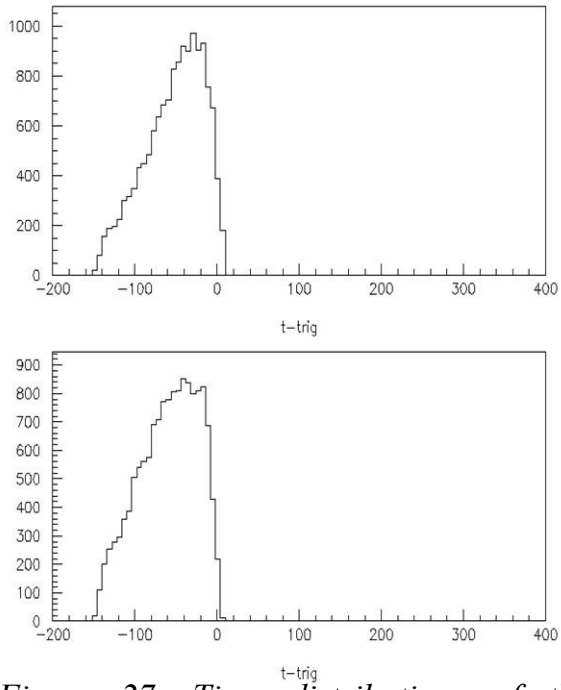

Figure 27. Time distributions of the signals of the tank that is together with the timing defining tank in the timing defining coincidence.

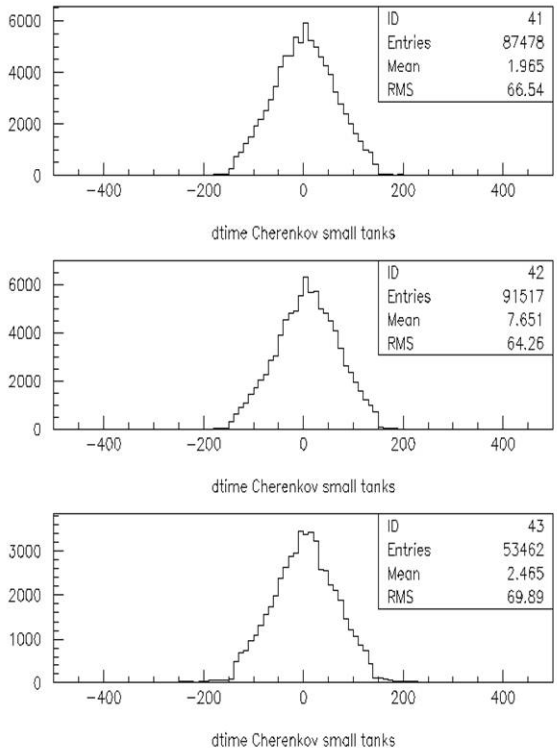

Figure 28. Time differences between the two PMTs of a same "on" tank (2 ADC channel cut).

Finally Figure 27 shows the distributions of the times of arrival of the signals in the second tank, that which is in the timing defining coincidence together with the first tank, and, again as expected, they arrive earlier than the signal which defines the timing of the trigger.

Figure 28 shows the distribution of the difference between the PMT times of a same "on" tank. Their root mean square values depend on the charge cut used to define "on" tanks as shown in Table 3 below. Factors contributing to these time differences include time slewing, which becomes less and less important as we increase the charge cut, photoelectron statistics and differences due to the geometry and the optics which imply that the different photons collected in each PMT have followed different paths (different attenuations in water, different absorptions in the wall).

The correlation between the PMT times of a same "on" tank is illustrated in Figure 29. Under the assumption of Gaussian uncertainties Δt_i , the rms value of the time difference distribution is $\Delta(t_{i1} - t_{i2}) = \sqrt{\Delta t_{i1}^2 + \Delta t_{i2}^2}$ while the uncertainty on the tank time measurement is $\Delta t_i = \frac{1}{2}\sqrt{\Delta t_{i1}^2 + \Delta t_{i2}^2} = \frac{1}{2}\Delta(t_{i1} - t_{i2})$

***Table 3**: Rms values of the time differences between the two PMTs of a same tank.*

Charge cut (ADC channels)	*Rms tank 1(ns)*	*Rms tank 2(ns)*	*Rms tank 3 (ns)*
2	*12.8*	*12.4*	*13.4*
10	*11.8*	*11.4*	*12.5*
18	*11.1*	*10.7*	*11.5*

We use this relation to evaluate the errors used in the Monte Carlo simulation to smear the tank times. We expect the Gaussian approximation to be good as there is so little correlation between the two PMT signals of a same tank. Yet, the uncertainties on these numbers, when they are interpreted in terms of measurement errors as they later are, are dominated by systematic errors resulting from the Gaussian approximation and from neglecting correlations. We estimate that the time measurement errors deduced from the numbers listed in Table 3 are evaluated with typical accuracies of ±0.8ns/12ns, namely ± 7% of their values.

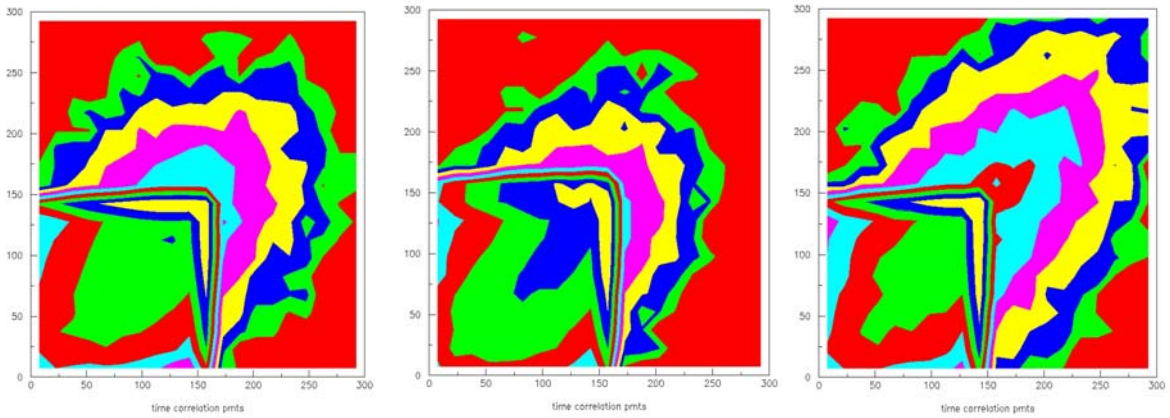

Figure 29. Correlations between the times of the two PMTs of a same "on" tank using a 2 ADC channel charge cut. The correlation appears as ellipses below the structure corresponding to the timing defining spikes. The shape of these structures corresponds to the distribution shown in Figure 25.

4.1.3 Multitank coincidences

Much care was taken to ensure that the ADC gate was large enough to fully contain any PMT signal associated with the trigger (whether early or late) and that the TDC time window was correspondingly sufficiently broad. Several checks were made to make sure that such was the case. The last step, having defined "on" tanks, is to

define double coincidence triggers as having at least two "on" tanks and triple coincidence triggers as having three "on" tanks. The time distribution between successive double coincidence triggers and triple coincidence triggers are shown in Figure 30. They are measured from a 10 kHz clock as has been described earlier. They are found to be exponential, as expected, but the scaler saturates at 6.4 s, corresponding to the capacity of its memory (64K), causing a small error on these distributions. The rates *R* (they are simply the reciprocals of the mean values of these distributions) are therefore measured by fitting exponentials of the form *exp(−Rt)* to the curves in Figure 30. They are listed in Table 4 below for charge cuts set at 2, 10 and 18 ADC channel respectively.

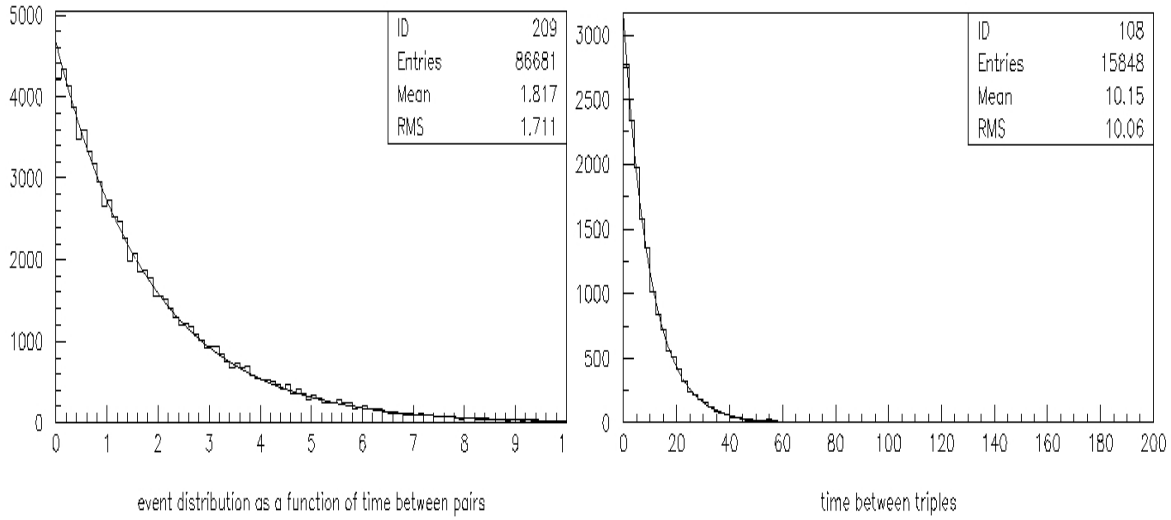

Figure 30. Time distribution between successive double (left panel) and triple (right panel) coincidences in seconds for a 2 ADC channel charge cut. The results of the exponential fits are indicated.

Also listed in Table 4 are the numbers of events in each sample. Note, however, that the rates quoted as "doubles" are for at least two tanks (possibly three) in coincidence while the number of events quoted as "doubles" are for two and only two. For example for a charge cut of 2 ADC channels, we have 70832 events having two and only two tanks in coincidence and 15849 events having three tanks in coincidence. We therefore have 15849+70832=86681 events having at least two tanks in coincidence. The rates evaluated from exponential fits to the distributions of the time between successive events, 0.54 and 0.098 Hz, correspond to the samples of 86681 and 15849 events respectively. Indeed 86681/0.54 and 15849/0.098 are equal, within errors, to the 44.8 hours that it took to collect the data sample. Precisely, the duration of the data collection (live time) calculated this way is 44.9, 44.8 and 44.8 hours from

the triple rates and for each charge cut separately. They are 44.6, 44.0 and 43.9 hours from the double rates. The small discrepancies, at a level of less than 2%, are within measurement errors. When comparing rates with the Monte Carlo we must be careful to compare exclusive rates with exclusive rates and inclusive rates with inclusive rates.

Table 4: *Triple and double rates (in Hz) evaluated as the slopes of the exponential fits to the time distributions of Figure 30 and similar. Also listed are the numbers of events corresponding to each configuration (see text).*

Cut	*Double rates (Hz)*	*Nr of events (doubles) 2-3/3-1/1-2/Sum*	*Triple rates (Hz)*	*Nr of events (triples) 1-2-3*	*Triple/ Double (%)*	*1-2/ Double (%)*
2	*0.54*	*15659/11935/43238/70832*	*0.098*	*15849*	*22.4*	*61.0*
10	*0.37*	*11306/8933/27045/47284*	*0.070*	*11297*	*23.9*	*57.2*
18	*0.25*	*7514/6259/17786/31559*	*0.049*	*7910*	*25.1*	*56.4*

4.2 Comparison with the predictions of the simulation

Figure 31 compares the *sinθ* distribution in the three-tank coincidence data sample with the Monte Carlo prediction using a value of 33^{o} for a_{θ}, the variance of the Gaussian zenith angle distribution. This distribution is essentially uncorrelated with the other quantities which we study in this section. Therefore, we keep the fine tuning of this parameter for later, once the measurement uncertainties attached to it will be better understood. We already commented in the preceding section on the reason causing most showers on which we trigger to be nearly vertical and we do not come back on this point here.

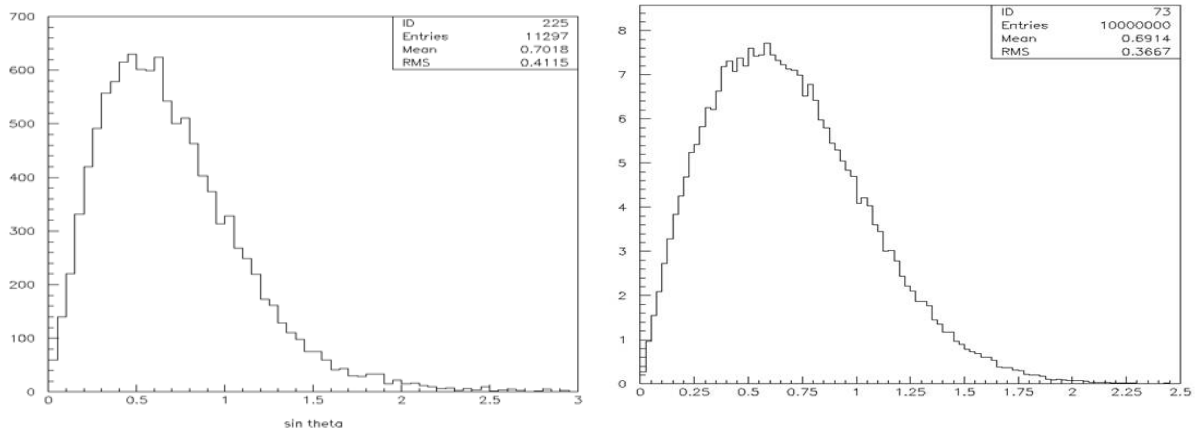

Figure 31. The sinθ distribution in real data (left panel) and simulation (right panel).

The α and β distributions measured in the three-tank coincidence data sample are shown in Figure 32 for a cut at 10 ADC channels. Their rms values, for each of the three values of the charge cut, are listed in Table 5 where they are compared with the predictions of the simulation. We remarked earlier that the uncertainty Δ_β on the β measurement is $(x_1-x_3)/(y_1-y_2)= 1.9$ times larger than that on the α measurement (Δ_α); moreover we expect from Relation 3.3 the real (no measurement errors) α and β distributions to have similar rms values (the azimuth distribution being nearly uniform); hence the difference between the rms values of the measured distributions gives us the measurement error. Precisely, we should have

$$\sqrt{Rms_\beta^2 - Rms_\alpha^2} = \sqrt{\Delta_\beta^2 - \Delta_\alpha^2} = \Delta_\alpha \sqrt{(1.9^2 - 1)} = 1.6\,\Delta_\alpha .$$

But as $\alpha=(t_3-t_2)/(x_3-x_1)$ we expect $\Delta_\alpha = Rms(t_3-t_2)/(871cm=29ns)$. Hence

$\Delta\alpha = \dfrac{\sqrt{Rms_\beta^2 - Rms_\alpha^2}}{1.6}$, which should be equal to $\Delta'\alpha = \dfrac{\sqrt{Rms_{t_3}^2 + Rms_{t_2}^2}}{29}$. These values are listed in the last two columns of Table 5 and display indeed a good agreement. This shows the validity of our evaluation of the measurement errors used in the Monte Carlo programme.

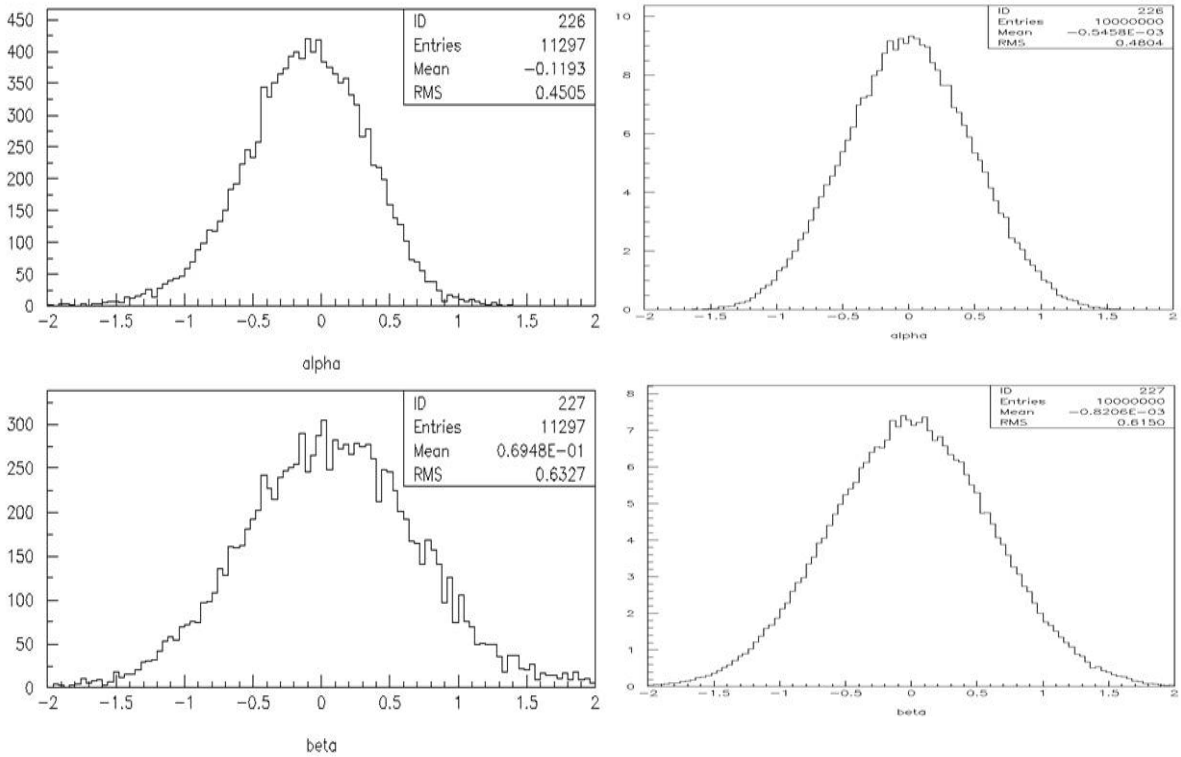

Figure 32. Comparison between the α and β distributions in the data (left panel) and in the simulation (right panel).

We also note, on Figure 32, that the α and β distributions have zero mean in the Monte Carlo simulation while, in the real data, they have mean values of −0.10 and 0.08 respectively. These correspond (see relation 3.3) to time offsets of $t_3 - t_2 = -3.0$ *ns* and $t_1 - t_2 = 1.2$ *ns* respectively. These values are within the accuracy with which the timing of the PMT signals was adjusted.

Table 5: *Time measurement errors*

Cut	*Rms α Data*	*Rms α Monte Carlo*	*Rms β Data*	*Rms β Monte Carlo*	Δ_α	Δ_α'
2	*0.49*	*0.53*	*0.69*	*0.66*	*0.30*	*0.31*
10	*0.45*	*0.48*	*0.63*	*0.62*	*0.28*	*0.29*
18	*0.41*	*0.45*	*0.59*	*0.58*	*0.27*	*0.27*

Having gained confidence in our evaluation of the measurement errors, we are now in a position to adjust a_θ for each of the three charge cuts by fitting the mean values of the experimental $sin\theta$ distributions. The results are summarized in Table 6.

Essentially, a_θ^2 is the difference between $Rms^2(\alpha)$ and $\Delta^2\alpha$ (see Table 5): the uncertainty on a_θ is therefore $\Delta^2\alpha\ \Delta(\Delta\alpha) / (a_\theta\ \Delta\alpha) = 0.07\Delta^2\alpha / a_\theta$. The uncertainties on a_θ listed in Table 6 have been increased to account for the differences between the predicted and experimental rms values of the α and β distributions; they are of the order of 2 to 4 degrees. The last column lists $\Delta\Omega = a_\theta^2$, an estimate of the solid angle over which the trigger detects vertical showers.

Table 6: *Fine tuning of the zenith angle distribution.*

Charge cut	*Data*			*Monte Carlo*				
	$<sin\theta>$	$Rms(\alpha)$	$Rms(\beta)$	$<sin\theta>$	$Rms(\alpha)$	$Rms(\beta)$	a_θ (^{o})	$\Delta\Omega$ (sr)
2	*0.78*	*0.49*	*0.69*	*0.76*	*0.53*	*0.66*	*37±4*	*0.42*
10	*0.70*	*0.45*	*0.63*	*0.69*	*0.48*	*0.61*	*33±2*	*0.33*
18	*0.65*	*0.41*	*0.59*	*0.65*	*0.45*	*0.58*	*30±2*	*0.27*

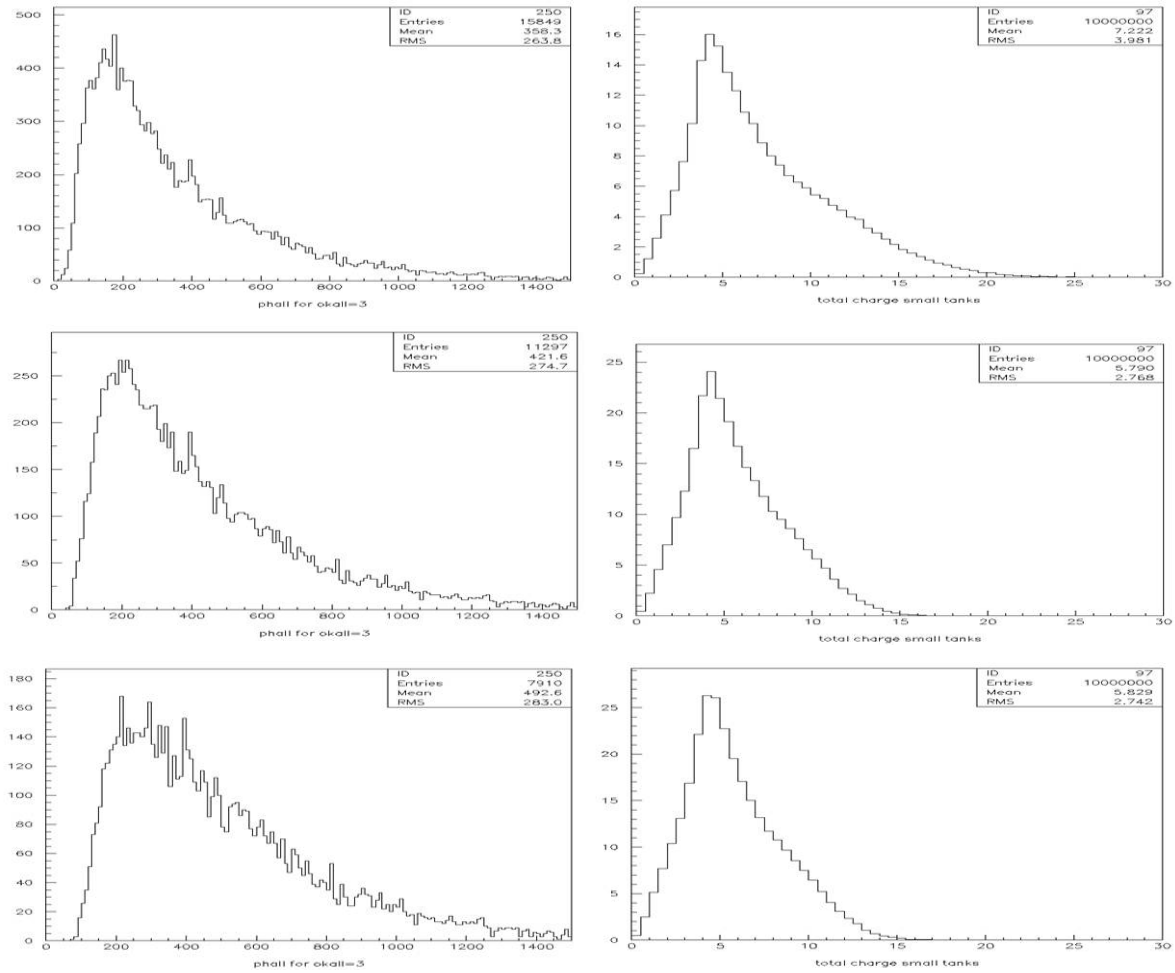

Figure 33.Total charge distribution collected in the small tanks for different charge cuts (from top to bottom, 2, 10 and 18 ADC channels). Data are shown on the left and the results of the Monte Carlo simulation on the right.

The total charge distributions, namely the sum of the three tank charges, are shown in Figure 33 for three-tank coincidences and for each of the three charge cuts separately. They are compared to the Monte Carlo distributions of the total number of shower particles hitting the three tanks. One would need to account for the response of the counters to a given particle in order to reproduce the data, including the detailed geometry and the energy distribution of the shower particles, mostly soft photons; however, this is well beyond the scope of the present study. But the simulation gives us an estimate of the effective number of shower particles hitting the three tanks, 6 on average. This is important information for further studies of the responses of the small tanks. Note however that this effective number has only a meaning within the framework of the model and its relation to the real number of particles of different kinds (electrons, photons and muons essentially) is not simple. Yet, we see that a

particle, as it is defined from our model, corresponds approximately to 50 ADC channels, which is very reasonable. Comparing the rate of increase of the mean total charge as a function of the charge cut, we see that going from an ADC cut of 2 to an ADC cut of 18 causes a 32% increase of the total charge in the data compared with 43% in the Monte Carlo simulation. Here again, the disagreement, which is due to the effect of the response, is not too large.

The double and triple rates listed in Table 4 were used to adjust the parameters m_0 and ρ_0 as illustrated in Figures 34 and 35. Table 7 summarizes the results. They correspond to particle densities in the shower core, $m_0/(2\pi\rho_0^2)$, between 2.5 and 3 m^{-2}.

The sensitivities of the two parameters m_0 and ρ_0 to the ratios $R_{12} = 1\text{-}2/\sum d$ and $R_{123} = 1\text{-}2\text{-}3/\sum d$ used to adjust them are measured in terms of the quantities $\sigma(R,x)=|dlogR/dlogx|$ where x stands for m_0 and ρ_0. They are nearly independent from the charge cut. Their values, $\sigma(R_{12}, \rho_0)=0.38$, $\sigma(R_{12}, m_0)=0.04$, $\sigma(R_{123}, \rho_0)=0.8$ and $\sigma(R_{123}, m_0)=0.80$ show the higher sensitivity of m_0 to R_{123}. They allow for an evaluation of the uncertainties attached to m_0 and ρ_0 once the errors on the ratios are known. We estimate the latter to be 2% on R_{123} and 4% on R_{12}.

***Table 7**: Tuning m_0 and ρ_0 to fit the data for different charge cuts.*

Charge cut	*Data*		*Monte Carlo*			
	1-2-3/∑d	*1-2/∑d*	*1-2-3/∑d*	*1-2/∑d*	m_0	ρ_0
2	*22.4%*	*61%*	*22.4%*	*61%*	*158 ±25*	*194 ±31*
10	*23.9%*	*57.2%*	*23.9%*	*57.2%*	*148 ±24*	*234 ±37*
18	*25.1%*	*56.4%*	*25.1%*	*56.4%*	*157 ±25*	*243±39*

From the simulation we find, using the same parameters, that the inclusive single tank rates should be about 11 times higher than the triple tank rates for a total charge cut of 2 ADC channels, namely of the order of 1 Hz. In fact they are in the 100 Hz range, some 100 times larger than this prediction. This is not surprising: they are dominated by muons which have a flux [21] of some 200 $m^{-2}s^{-1}$ when integrated over solid angle. This implies that the small tanks have an effective area of only 0.5 m^2 for detecting muons, namely that their detection efficiency to muons is only 20% or so (see Figure 18). Indeed, their geometry is not well adapted to muon detection (contrary

to that of the big tank) and their optical properties are poor (no wall coating). The contribution to the single tank rates of showers producing a three-tank coincidence is at the percent level. Again, this is not surprising as 92% of the muons are known to be isolated and the triple coincidence requirement is much more demanding than simply requiring non-isolation.

From the measured triple coincidence rates, 0.098, 0.070 and 0.049 Hz for each of the three charge cuts, we can calculate the flux of detected showers by dividing by the proper Monte Carlo weights, 21.6, 26.1 and 29.2 m^2 respectively. The results are 4.5 10^{-3}, 2.7 10^{-3} and 1.7 10^{-3} $m^{-2}s^{-1}$ respectively. Approximating the differential primary flux of Figure 1 by the expression $0.1(E_{GeV}/100)^{-2.7}$ $m^{-2}s^{-1}sr^{-1}GeV^{-1}$ we find, after integration over energy and multiplication by the solid angle $\Delta\Omega$ (see Table 6) a primary flux, integrated above the rigidity cut-off, of respectively 50, 40 and 32 $m^{-2}s^{-1}$, namely 1.1, 1.5 and 1.9 10^4 times higher than detected. Conversely, if all primaries having energies in excess of E_0 would produce detectable showers, one would need E_0 to be as high as 6.2, 11 and 13 TeV respectively. The reality is between these two extremes: the detected showers must have energies between 17 GeV and these high multiTeV values. Their energy distribution is governed by the competition between the energy dependence of the flux and the fluctuations in the tail of the longitudinal shower profile. A reliable evaluation is extremely difficult in such conditions and well beyond the scope of the present study. A crude qualitative estimate can nevertheless be obtained as follows: the longitudinal profile (Relation 1.1) is dominated in the tail by the exponential factor and, as X_{max} varies only logarithmically with energy, its energy dependence is governed by that of $S(x)$, and hence it is proportional to energy. In a range where logarithmic variations can be neglected, the probability to detect a shower of energy E must therefore take the form P_0E where P_0 is a small, but constant, probability density (in GeV^{-1}). The mean value of the energy of detected showers can then easily be calculated between the limits of 17 GeV and 16, 19 or 22 TeV: the result is 190, 230 and 250 GeV respectively. Above 190 GeV, the primary flux is 1.4 $m^{-2}s^{-1}$ giving a probability of about 3‰ for a shower to be detectable. This result is qualitative: it is only meant to give an idea of the kind of showers which the detector triggers on.

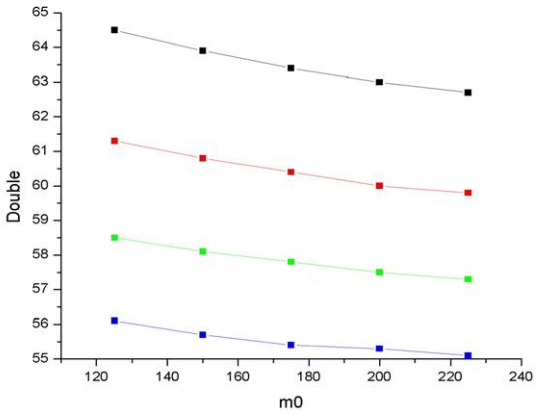

Figure34. Dependence of the predicted value of R_{12} on m_0 and ρ_0 for a charge cut of 10 ADC channels. The curves correspond to different values of ρ_0 (175, 200, 225 and 250 from top to bottom).

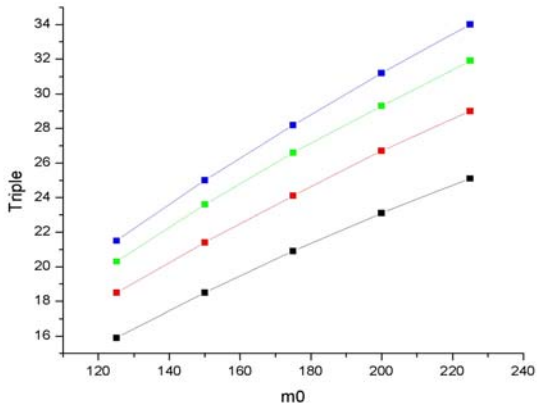

Figure35. Dependence of the predicted value of R_{123} on m_0 and ρ_0 for a charge cut of 10 ADC channels. The curves correspond to different values of ρ_0 (175, 200, 225 and 250 from top to bottom).

4.3 Response of the main tank to the triple coincidence trigger

From triple coincidence simulated events, we can evaluate the probability of having a signal in the main tank in the same way as we did for the small tanks. As the main tank is much larger than the small tanks[2] and located centrally, we expect essentially each triple coincidence trigger to give a signal in the main tank. Indeed, the expected probability of having a signal in the main tank for triple coincidence triggers has a very high mean value, 93%.

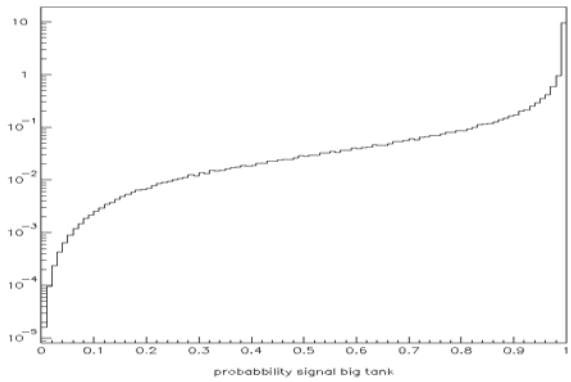

Figure36. Predicted distribution of the probability (in % per 0.01 bin) of having a signal in the main tank for triple coincidences of the small tanks.

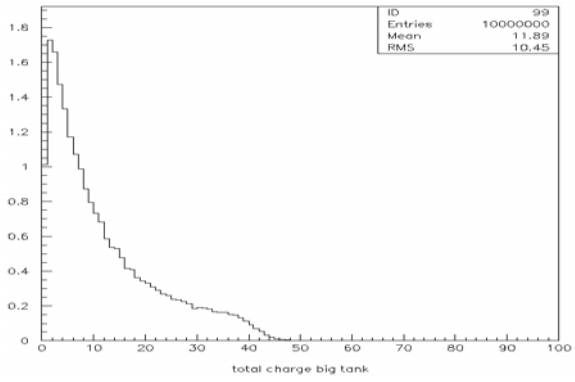

Figure37. Predicted distribution of the number of particles hitting the main tank for triple coincidences of the small tanks

[2] In practice, for this reason, the calculation was made by fragmenting the volume of the main tank in eight pieces having equal areas.

Its distribution is illustrated in Figure 36 and that of the mean number of particles hitting the main tank is shown in Figure 37. On average, twelve particles hit the main tank. This prediction is corroborated by the data as illustrated in Figure 38 where the main tank charge, defined as the mean value of the three PMT charges, is displayed for each of the three charge cuts applied to the small tanks (2, 10 and 18 ADC counts respectively). One particle in the model corresponds to 7.5 ADC counts per PMT (22.5 ADC counts in total) in the data. It is remarkable that the measured main tank charge increases significantly with the charge cut in the small tanks.

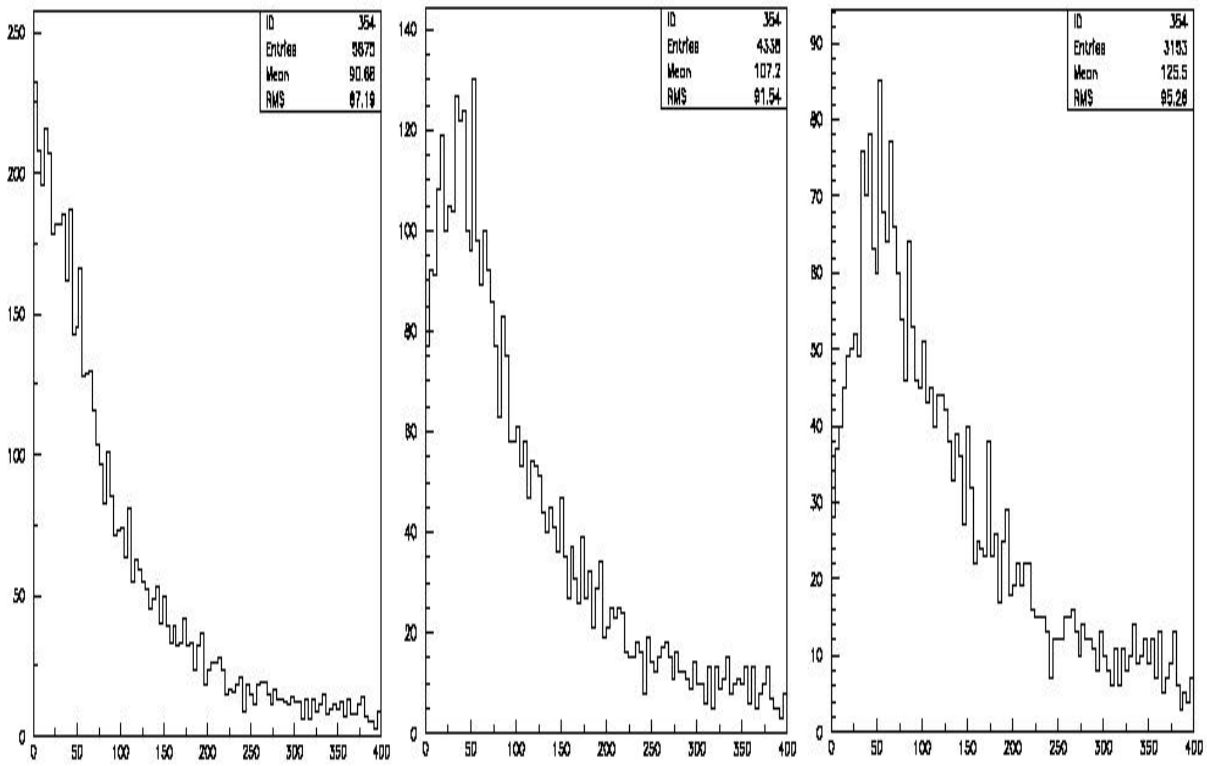

Figure 38. Mean charge of the main tank measured for triple coincidences of the small tanks with charge cuts set at 2, 10 and 18 ADC channels (from left to right).

Similarly, the main tank timing is defined as the mean value of the three PMT timings and its distribution is shown in Figure 39. Here, we have used the anode signals to measure the charges and the dynode signals to measure the times. For each of these quantities, charge and time, we define for each PMT its deviation from the mean, Δq_i and Δt_i respectively. By definition, the sum of the three Δq_i (or Δt_i) of a same tank is zero. We can then plot them in a two-dimensional figure (Dalitz plot), on three axes at 120^o from each other. This is done in Figures 40 and 41, displaying a clear correlation between the signals recorded by the three PMTs of the main tank.

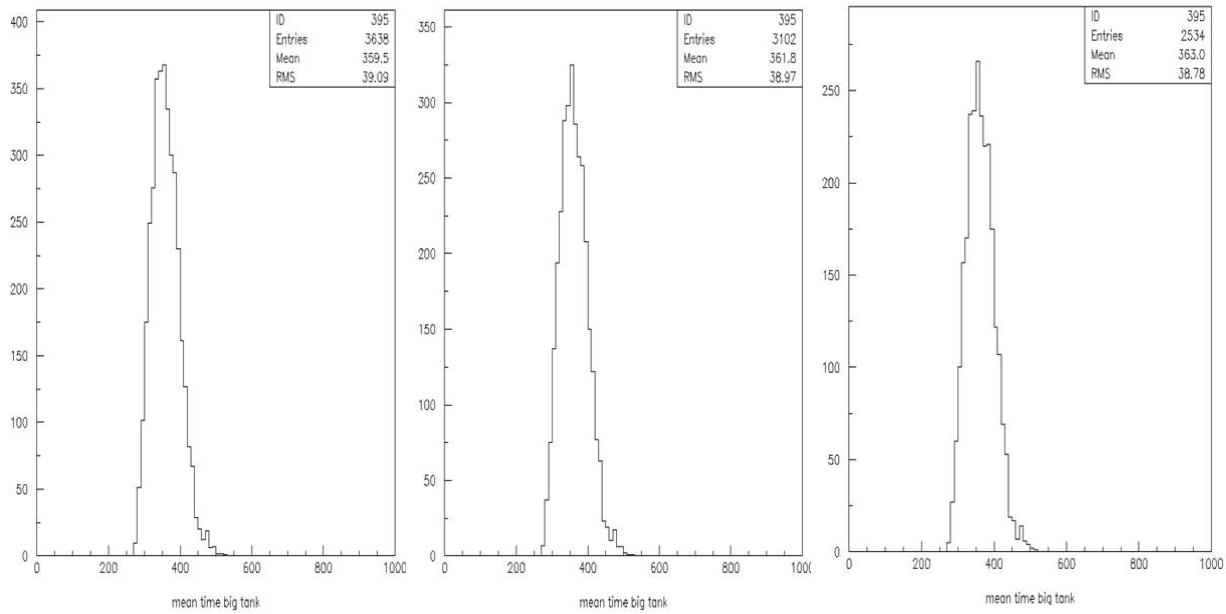

Figure39 . Mean time of the main tank measured for triple coincidences of the small tanks with charge cuts set at 2, 10 and 18 ADC channels (from left to right).

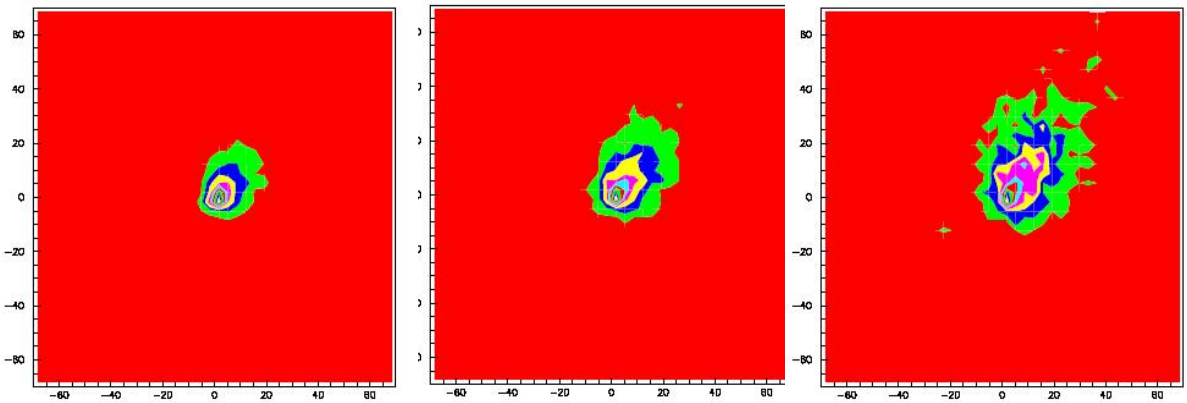

Figure 40. Correlation between the charges measured in each of the three PMTs of the main tank for triple coincidences of the small tank with charge cuts set at 2, 10 and 18 ADC channels (top to bottom).

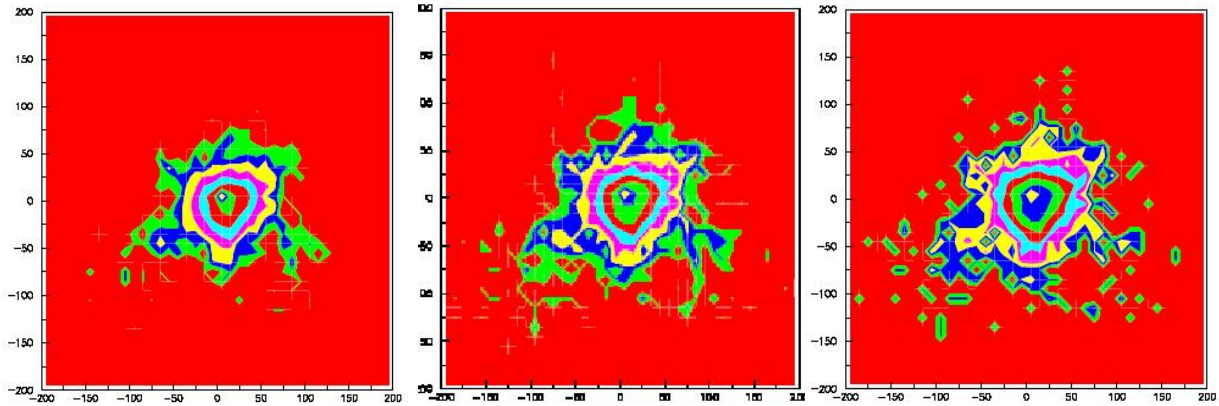

Figure 41. Correlation between the times measured in each of the three PMTs of the main tank for triple coincidences of the small tank with charge cuts set at 2, 10 and 18 ADC channels (top to bottom).

To see it more quantitatively we show in Figures 42 and 43 the distributions of asymmetries defined as $\sqrt{(\sum \Delta q_i^2 / \langle Q \rangle^2)}$ and $\sqrt{(\sum \Delta t_i^2 / \langle T \rangle^2)}$ respectively. Here $\langle Q \rangle$ is the average value of the sum of the charges of the signals of the three PMTs and $\langle T \rangle$ that of their times of arrival. The charge asymmetries are between 9% and 15% while the time asymmetries are between 2% and 3 %. These low values provide evidence for the good quality of the three-tank trigger as well as of the optical properties of the refurbished main tank.

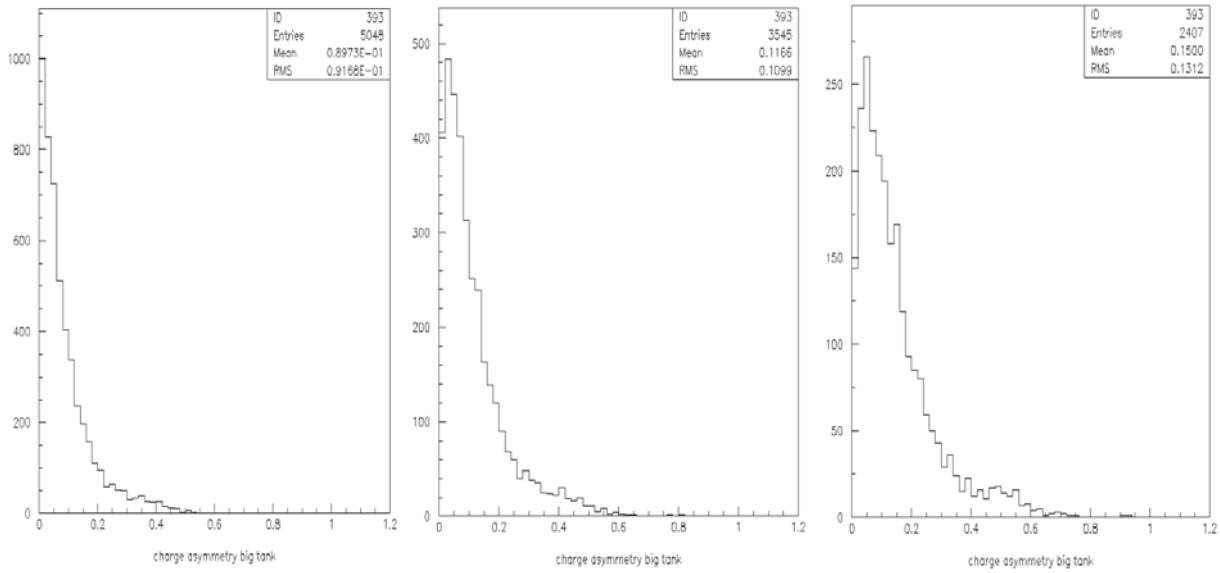

Figure 42. Distributions of the charge asymmetry between the three PMTs of the main tank defined as $\sqrt{(\sum \Delta q_i^2 / \langle Q \rangle^2)}$ for triple coincidences of the small tanks with charge cuts of 2, 10 and 18 ADC channels (from left to right).

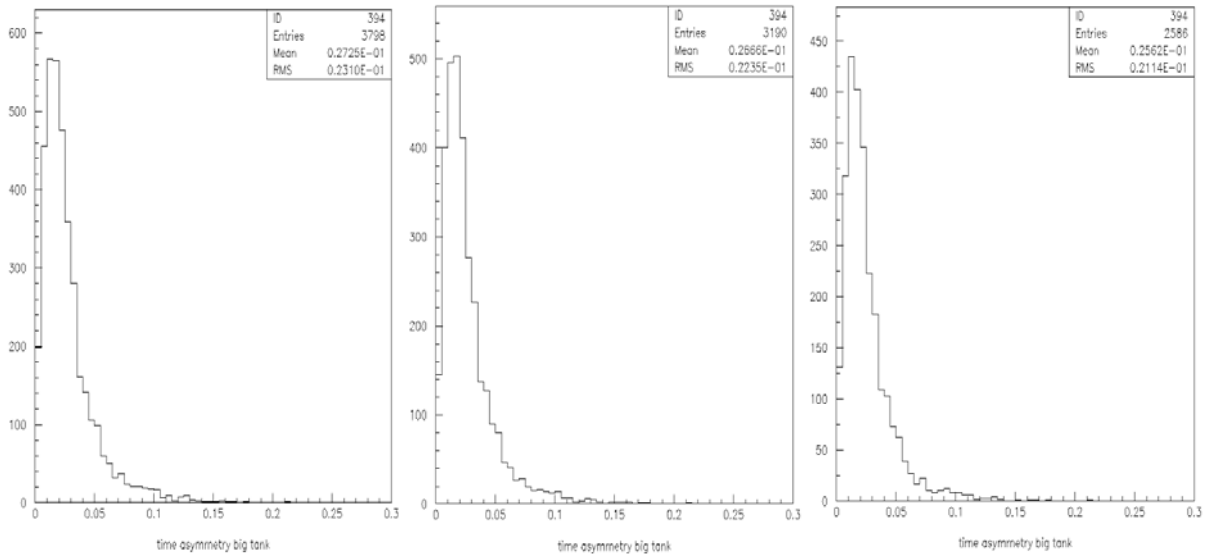

Figure 43. Distributions of the time asymmetry between the three PMTs of the main tank defined as $\sqrt{(\sum \Delta t_i^2 / \langle T \rangle^2)}$ for triple coincidences of the small tanks with charge cuts of 2, 10 and 18 ADC channels (from left to right).

5. SUMMARY AND PERSPECTIVES

We have operated and studied a set of three Cherenkov counters having the ability to detect extensive air showers. These counters are installed on the roof of VATLY, a cosmic ray laboratory in Hanoi, with the aim to provide a trigger for the study of a large Cherenkov counter around which they are located. The latter is a replica of a surface detector of the Pierre Auger Observatory, which we have constructed, assembled and operated.

After an introduction describing our aim and strategy, and after having presented the main features of the hardware and of the experimental method, we have given a detailed account of data collected using this trigger. We have been particularly attentive to devise checks providing evidence for the proper operation of the system.

In order to better understand the main features of the showers on which we trigger, we have produced a simple simulation of the detector using an ad hoc effective model which requires only three parameters. One of them fixes the zenith angle distribution while the two others, ρ_0 and m_0 , measure the radius of the shower core and the total particle multiplicity. The relation between the latter and the real photon densities (energy density and number density) is far from being simple; the model nevertheless provides a useful comparison with the data. It has made it possible to reach a number of conclusions:

− The three-tank coincidence trigger rate is of the order of 0.1 Hz. The acceptance of this trigger, obtained from the model, is of the order of 22 $m^{2.}$. The flux of showers that can be selected by the trigger is therefore of the order of 5 10^{-3} $m^{-2}s^{-1}$, a factor 10^4 lower than the integrated primary flux.

− At the price of reducing the number of events retained as three-tank triggers, it is possible to select events with larger charges in each of the three small tanks, resulting in improved measurement accuracy. For example, a reduction of the sample by a factor of 2 allows for a 15% improvement in the precision of the time measurements. Throughout the study, we have given results obtained for three different such data samples.

− The trigger selects vertical showers over an effective solid angle of the order of 0.4 sr. Fitting the zenith angle distribution to a Gaussian gives a variance of 37^o. It is already difficult for vertical showers to survive after having traversed 1kg/cm^2 of atmosphere; it becomes quickly impossible for inclined showers: this explains why we select nearly vertical showers.

− Qualitatively, we expect the showers on which we trigger to have energies in the 200 GeV range and a few per mil probability of surviving at sea level with a sufficient energy density.

− Within the framework of the model used, the shower cores on which we trigger have typical particle densities of 2.5 to 3 m^{-2} and typical radii of 2 m. In real life, it is rather the energy density of soft photons that is relevant and its relation with ρ_0 and m_0 is complex and has not been investigated here.

− Nearly each three-tank trigger is associated with a signal in the main tank: the trigger perfectly fulfils the task for which it was designed. Moreover, strong correlations between the signals of the three PMTs of the main tank provide evidence for a very significant improvement of the quality of its optical properties after having been refurbished.

The availability of such a trigger will open the door to a number of new studies.

Concerning the three-tank system, a refined analysis of larger data samples will make it possible to give a more quantitative evaluation of the shower energy and energy density on ground. It may also be possible to measure the muon to electron ratio.

Concerning the main tank, a detailed study of its response to soft photons will now become possible. Calorimetric measurements below the tank would help refining the evaluation of the shower energies and their implementation should be considered. An energy calibration of the counter in terms of vertical muon equivalents (VEM) should now become feasible.

REFERENCES

[1] P.T.T. Nhung, Master thesis, 2006, Hanoi National University, *"Performance studies of water Cherenkov counters"*.

[2] P.N. Dông, Master thesis, 2006, Hanoi University of Technology, "*The Cherenkov counters of the VATLY laboratory*".

[3] M.S. Longair, *High Energy Astrophysics,* Cambridge University Press, 1992.

[4] T.K. Gaisser *et al*., *Cosmic Rays and Particle Physics,* Cambridge University Press, 1990.

[5] L. Anchordoqui *et al*., *High Energy Physics in the Atmosphere: Phenomenology of Cosmic Ray Air Showers,* NUB-3245/Th-04, La Plata-Th-04-03, hep-ph/0407020.

[6] H, Muraishi *et al*., Prog.Theor.Phys. 113 (2005) 721-731.

[7] K. Greisen, Phys. Rev. Lett. 16, 748 (1966).

[8] G. T. Zatsepin and V. A. Kuzmin, JETP Lett. 4, 78 (1966) [Pisma Zh. Eksp. Teor. Fiz. 4, 114 (1966)].

[9] K. Sakurai, *Physics of Solar Cosmic Rays,* University of Tokyo Press, 1974.

[10] G. Rowell, Journal of Phys.: Conference Series 47 (2006) 21–30.

[11] D. Harari *et al*., *Correlation of cosmic rays with astronomical objects in the Pierre Auger Observatory data*, Auger Note GAP-2006-046 (2006).

[12] J.D.Hague *et al*., *Search for Correlations between nearby AGNs and Auger data*, Auger Note GAP-2006-047 (2006).

[13] The Auger Collaboration, Nucl. Instr. Meth. A 523, 50 (2004), and references therein.

[14] P.N.Diep et al., Comm. Phys., Volume 16-3 (2006) 129-143.

P.N. Diep, Master thesis, 2006, Institute of Physics and Electronics, "*Detection and study of ultra high energy cosmic rays"*.

[15] R.M. Baltrusaitis et al., Nucl. Inst. Meth. A240 (1985) 410,

D. Bird et al., Nucl. Inst. Meth., A349 (1994) 592,

D. Bird et al., Astrophys. J. 424 (1994) 491,

G. Davidson and R. ONeil, J. Chem. Phys. 41 (1964) 3946.

[16] P. Sokolsky, Am. Inst. Phys. Conf. Proc., 433 (1998) 65.

[17] T. K. Gaisser and A. M. Hillas, Proc. of 15th International Cosmic Ray Conference, Plovdiv 8, 353 (1977).

[18] T. K. Gaisser, AIP Conf. Proc. 558 (2001) 27.

[19] S. Eidelman *et al.*, Phys. Lett. B592 (2004) 1,

W. R. Leo, *Techniques for Nuclear and Particle Physics Experiments*, Springer Verlag, 1994.

[20] A. Haungs, Kascade Collaboration, ANI 99 workshop, May-June 1999, Nor Amberd Station, Mt Aragats, Armenia.

[21] P.N.Dinh et al., Nucl. Phys. B 627 (2002) 29 - 42.

[22] P.N.Dinh et al., Nucl. Phys. B 661 (2003) 3 - 16.

[23] P.N.Diep et al., Comm. Phys., Vietnam 14, 2003, p57.

P.N.Diep, Diploma , 2003, Hanoi National University, "*Dependence of the cosmic muon flux on atmospheric pressure"*.

P.T.Nhung, Diploma, 2003, Hanoi National University, "*Dependence of the cosmic muon flux on atmospheric temperature"*.